Tooth acellular extrinsic fibre cementum incremental lines in humans are formed by parallel branched Sharpey's fibres and not by its mineral phase

Lourdes Couoh, Lauro Bucio, José Luis Ruvalcaba, Britta Manoel, Tengteng Tang, Aurélien Gourrier, Kathryn Grandfield

Journal of Structural Biology 216 (2024) 108084

Contents lists available at ScienceDirect

Journal of Structural Biology

journal homepage: www.elsevier.com/locate/yjsbi

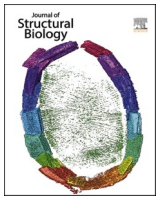

Research Article

Tooth acellular extrinsic fibre cementum incremental lines in humans are formed by parallel branched Sharpey's fibres and not by its mineral phase

Lourdes R. Couoh [a,*], Lauro Bucio [b], José Luis Ruvalcaba [c], Britta Manoel [d,e], Tengteng Tang [f], Aurélien Gourrier [g], Kathryn Grandfield [f,h,*]

[a] Dirección de Antropología Física, Instituto Nacional de Antropología e Historia, Paseo de la Reforma y Gandhi, Chapultepec Polanco 11560, CDMX, México
[b] Laboratorio de Cristalofísica y Materiales Naturales, Instituto de Física, Universidad Nacional Autónoma de México, Ciudad Universitaria, Coyoacán 04510, CDMX, México
[c] Laboratorio Nacional de Ciencias para la Investigación y Conservación del Patrimonio Cultural, Instituto de Física, Universidad Nacional Autónoma de México, Ciudad Universitaria, Coyoacán 04510, CDMX, México
[d] European Synchrotron Radiation Facility, 71 Avenue des Martyrs 38000, Grenoble, France
[e] Bruker AXS Advanced X-ray Solutions GmbH, Östliche Rheinbrückenstraße 49 76187, Karlsruhe, Germany
[f] Department of Materials Science and Engineering, McMaster University, Hamilton L8S 4L7, ON, Canada
[g] Univ. Grenoble Alpes, CNRS, LIPhy, Grenoble F-38000, France
[h] School of Biomedical Engineering, McMaster University, Hamilton L8S 4L7, ON, Canada

ARTICLE INFO

Edited by Elia Beniash

Keywords:
Tooth cementum annulations
Acellular Extrinsic Fibre Cementum (AEFC)
Synchrotron scanning (SAX, XRD, XRF)
FIB-TEM
PFIB-SEM
FIB-ETOMO
Sharpey's fibres

ABSTRACT

In humans, the growth pattern of the acellular extrinsic fibre cementum (AEFC) has been useful to estimate the age-at-death. However, the structural organization behind such a pattern remains poorly understood. In this study tooth cementum from seven individuals from a Mexican modern skeletal series were analyzed with the aim of unveiling the AEFC collagenous and mineral structure using multimodal imaging approaches. The organization of collagen fibres was first determined using: light microscopy, transmission electron microscopy (TEM), electron tomography, and plasma FIB scanning electron microscopy (PFIB-SEM) tomography. The mineral properties were then investigated using: synchrotron small-angle X-ray scattering (SAXS) for *T*-parameter (correlation length between mineral particles); synchrotron X-ray diffraction (XRD) for *L*-parameter (mineral crystalline domain size estimation), alignment parameter (crystals preferred orientation) and lattice parameters *a* and *c*; as well as synchrotron X-ray fluorescence for spatial distribution of calcium, phosphorus and zinc. Results show that Sharpey's fibres branched out fibres that cover and uncover other collagen bundles forming aligned arched structures that are joined by these same fibres but in a parallel fashion. The parallel fibres are not set as a continuum on the same plane and when they are superimposed project the AEFC incremental lines due to the collagen birefringence. The orientation of the apatite crystallites is subject to the arrangement of the collagen fibres, and the obtained parameter values along with the elemental distribution maps, revealed this mineral tissue as relatively homogeneous. Therefore, no intrinsic characteristics of the mineral phase could be associated with the alternating AEFC incremental pattern.

1. Introduction

Tooth roots are surrounded and covered by cementum, which is one of the four mineralized tissues found in humans. *Homo sapiens*, like all mammals and crocodilians, has a *thecodonty* type of tooth implantation, which means that the tooth root is within a deep socket of alveolar bone, firmly anchored to this by the periodontal ligament (PDL) (Bertin et al., 2018; LeBlanc & Reisz, 2013). The PDL has a complex architecture that is formed primarily by collagen fibrils organized in bundles and fibres (Hirashima et al., 2020a; Ho et al., 2010; McCulloch et al., 2000), which thickness, quantity and orientation depend on their location along the tooth root (de Jong et al., 2017; Grant & Bernick, 1972; Hirashima et al., 2020b). PDL's collagen organization has a direct relationship to the different types of tooth cementum, which according to its function and location, can be differentiated mainly by the presence or absence of embedded cementocytes, as well as by the origin of the collagen fibres,

* Corresponding authors.
E-mail addresses: lourdes_couoh@inah.gob.mx (L.R. Couoh), kgrandfield@mcmaster.ca (K. Grandfield).

https://doi.org/10.1016/j.jsb.2024.108084
Received 23 November 2023; Received in revised form 28 February 2024; Accepted 10 March 2024
Available online 11 March 2024

which are mineralized by hydroxyapatite crystals (Bosshardt, 2005; Bosshardt & Schroeder, 1991, 1992; Bosshardt & Selvig, 1997; Yamamoto et al., 2000, 2016).

In this sense, the *acellular extrinsic fibre cementum* (AEFC) is referred to as this because the collagen fibres (at this point also known as Sharpey's fibres) come from the PDL and has only extracellular matrix components and mineral (Hand & Frank, 2014). *Cellular intrinsic fibre cementum* (CIFC) has forming cells that are responsible for secreting and controlling the intrinsic collagen fibrils (Bosshardt & Schroeder, 1992; Yamamoto et al., 2016) (Fig. 1). Nevertheless, often CIFC also contains extrinsic fibres and hence, depending on their quantity, CIFC is subdivided into different types, *e.g.*, *cellular mixed stratified cementum* (CMSC) (Yamamoto et al., 2016). The covering range of AEFC varies among types of teeth, but in general it can be found from the cervical half to two-thirds of the root surface, while CIFC takes place in the apical one-third to one-half of a single-rooted tooth or furcation areas of multi-rooted tooth (Hand & Frank, 2014; Hirashima et al., 2020c; Yamamoto et al., 2016).

All cementum types grow by apposition throughout life (Bosshardt & Schroeder, 1996), *i.e.*, the growth takes place by forming new layers upon the surface of pre-existing layers. Neither CIFC nor AEFC experience turnover and remodeling like bone, although CIFC has a limited role as reparative or regenerative tissue (Raspanti et al., 2000; Yamamoto et al., 2016). CIFC and AEFC express a pattern of incremental markings (appearing as alternate dark and translucent bands) when examined with polarized transmitted light microscopy (Fig. 1). However, due to the differences between these two cementum types (as the rate of growing and structural organization) the appearance of such a pattern is different and specific for each one (Bosshardt, 2005; Bosshardt & Schroeder, 1992; Bosshardt & Selvig, 1997; Yamamoto et al., 2010). For CIFC the mineralized collagen fibres are displayed as an alternating lamellar pattern, similar to the "twisted plywood" model for bone (Giraud-Guille, 1988; Yamamoto et al., 2010, 2016). While for AEFC, although it has been identified that the mineralized Sharpey's fibres, or collagen bundles, are arrayed in a parallel fashion between them (oriented perpendicularly towards the tooth axis) (Bosshardt & Schroeder, 1991; Bosshardt & Selvig, 1997), with some collagen fibres running in a parallel direction towards the root surface —sometimes linked by anastomosis— (Aboulfadl & Hulliger, 2015; Catros et al., 2008; Colard et al., 2016; Furseth, 1974; Kvam, 1973; Raspanti et al., 2000; Yamamoto et al., 2016), it is still unknown if the AEFC's mineralized collagen architecture contributes to form the incremental alternating pattern noted above.

In humans, AEFC's growth pattern has been related to a circannual biological rhythm, and disciplines as physical anthropology have found this useful to estimate the age-at-death of individuals from present and past populations (Bertrand et al., 2019; Couoh, 2017; Naji et al., 2016; Naji, Rendu, et al., 2022). In order to provide the scientific support to this latter understanding, various scholars have made individual approaches and launched different hypotheses unraveling the structural and/or compositional reasons that produce the above incremental marking on AEFC (e.g., Colard et al., 2016; Cool et al., 2002; Dean et al., 2018; Lieberman, 1994). In this respect, some advances have been made, but are as yet inconclusive, considering the distribution of zinc, calcium and strontium as a clear marker of the incremental growth (Dean et al., 2018; Naji, Stock, et al., 2022).

In this sense, using different state-of-the-art analytical and microscopic techniques, the aim of the present study is to identify the structural organization of AEFC and some of its mineral properties. The specific objectives addressed are: 1) To identify the collagen fibres orientation within AEFC to unravel its architecture. 2) To determine if size, orientation, alignment and lattice parameters of the hydroxyapatite crystals are related to incremental growth pattern. 3) To examine if the distribution of elements like Ca, P and Zn are consistent with the incremental marking.

2. Material and methods

The tooth cementum samples used in this study are taken from the Mexican skeletal series *San Nicolás Tolentino*, which is composed of individuals who died in the last two decades of the 20th century. The skeletons were uncovered from four cemeteries located within Mexico City: *San Nicolás Tolentino*, *20 de Noviembre*, *Pueblo de Los Reyes*, and *Dolores*. This skeleton series is stored and protected by the National Institute of Anthropology and History of Mexico [INAH], who authorized the extraction of one tooth per each of the seven individuals included in the sample of this study (Official Dispatch Number: 401-B(4) 19.2015/361389). The selected sample is comprised of tooth cementum taken from four canines and three premolars from individuals with different ages, ranging from 20 to 92 years (Table 1).

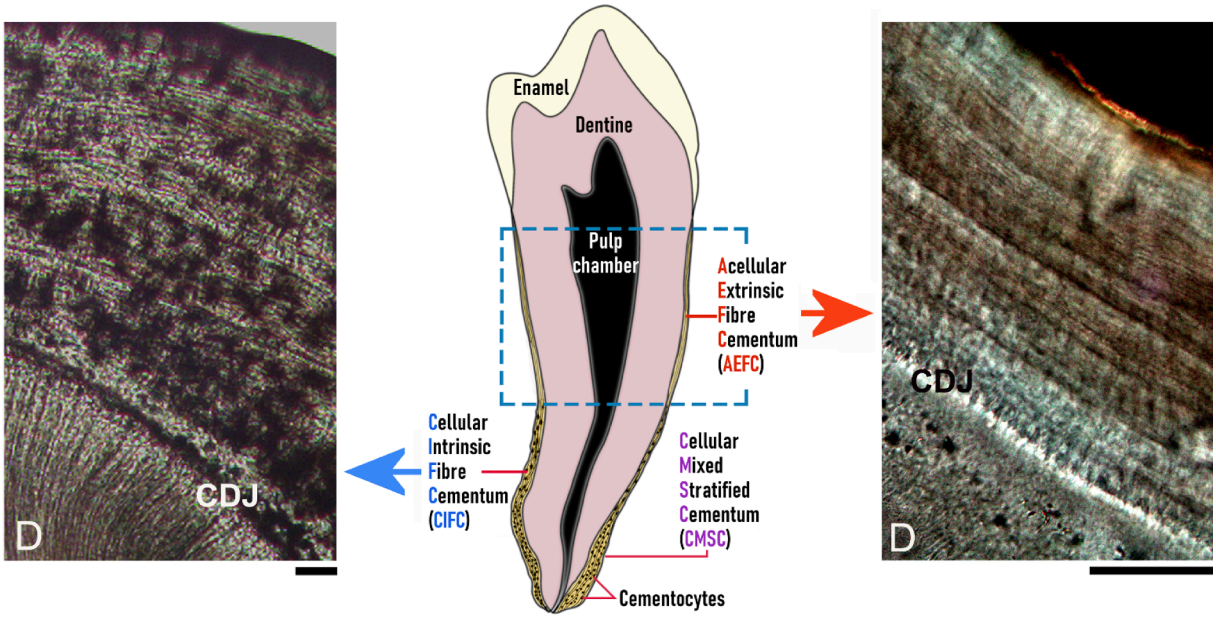

Fig. 1. Positioning of the main cementum types along the tooth root. The incremental lines growth pattern is shown for AEFC and CIFC. Abbreviations: D, *dentine;* CDJ, *cemento-dentinal-junction.* Scales are 50 μm.

Table 1
List of samples.

Sample ID	Skeleton reference label	Cemetery	Sex	Age-at-death[†]	Tooth type
HATC-65	PR-2	*Pueblo de los Reyes*	M	20	Upper right canine
HATC-12	SNT-38	*San Nicolás Tolentino*	M	26	Lower right canine
HATC-26	SNT-60	*San Nicolás Tolentino*	M	30	Upper left canine
HATC-13	SNT-43	*San Nicolás Tolentino*	M	42	Lower left first premolar
HATC-27	SNT-63	*San Nicolás Tolentino*	F	55	Lower left canine
HATC-48	DOL-23	*Dolores*	M	71	Lower left second premolar
HATC-05	SNT-6	*San Nicolás Tolentino*	F	92	Lower right first premolar

[†] The chronological ages were recorded from civil records, except for HATC-48 which age was estimated by *tooth cementum annulations* method in Couoh (2017).

The sample preparation was dependent on the experiment to be conducted (see Suppl. Mat. 1 for the complete procedures) and not all samples were analyzed with the same techniques (Suppl. Mat. 3 Table S1). In all cases cross-sections were taken from AEFC, within the middle third of the root. In addition, for comparative purposes, cross-sections from CIFC at the lower third of the root were sampled in four cases, as well as one from CMSC in one of these. According to the techniques used, in Fig. 2 is presented a summary of the sections taken from AEFC.

Light microscopy (LM). All cross-cut sections were examined with different light microscopy techniques, such as polarized, transmitted, and reflected light, as well as differential interference contrast (Zeiss® Axioplan 2, Carl Zeiss Pty Ltd, Göttingen, Germany). The images were acquired with a Clemex® camera along with the software Clemex Vision Lite® (Clemex, Quebec, Canada).

Transmission electron microscopy (TEM). All samples remained untreated (except for one that was demineralized and stained by successive treatments with osmium tetroxide and thiocarbohydrazide (OTOTO protocol (Reznikov et al., 2013, 2014)) and were prepared to be sectioned with the ultramicrotome. These samples were placed on Cu grids and viewed in a JEOL JEM 1200 EX TEMSCAN transmission electron microscope (JEOL, Peabody, MA, USA) operated at an accelerating voltage of 80 kV. Bright-field (BF) images were acquired with an AMT 4-megapixel digital camera (Advanced Microscopy Techniques, Woburn, MA, USA). On the other hand, for a higher resolution analysis, two samples (HATC-13 and HATC-48) were selected to produce TEM lamellae with a dual-beam FIB. A Zeiss NVision40 FIB equipped with a Ga^+ beam operated at 30 kV, a tungsten gas injector system and Kleindiek micromanipulator drive system were used to produce four lamellae through an *in situ* lift-out method (Suppl. Mat. 2 Figure S1) (Grandfield et al., 2018; Grandfield & Engqvist, 2014). From the cross-sections surfaces of each specimen, one lift-out oriented longitudinally was obtained; and from the tooth root external surface two lift-outs were taken from HATC-13, one oriented longitudinally and the other transversally (Fig. 2). All FIB-prepared TEM samples were carbon-coated (~5 nm) and imaged in a FEI Titan 80/300 field emission scanning transmission electron microscope (STEM), operated at 300 kV. Higher-resolution images with compositional contrast were obtained in high-angle annular dark-field (HAADF) STEM mode. Intensity in the HAADF images is approximately proportional to Z^2 (Z = atomic number); therefore high-Z regions, such as minerals, appear brighter. In addition, two of the FIB-prepared TEM samples were viewed using the field emission JEOL 2010F TEM/STEM operated at 200 keV. Higher-resolution images with annular bright-field (ABF) STEM mode were acquired.

Electron Tomography. A linear axis tilt scheme over 108° (from + 48° to −60°) was used on one of the lamellae prepared by FIB (from the cross-section surface on HATC-13) for electron tomography with the Model 2020 Advanced Tomography Holder (E.A. Fischione Instruments, Inc., Export, PA) on a FEI Titan 80/300, operated at 300 keV. HAADF STEM images were recorded every 2° with the automated focusing, image shifting, and acquisition by the Inspect 3D software (ThermoFisher Scientific, Netherlands). Automated Fourier filtered cross-correlation and manual alignment of the tilt axis were used to align the images of the tilt series using the software Explore3D™ (ThermoFisher Scientific®). Reconstructions were produced with a simultaneous iterative reconstruction technique (SIRT) with 20 iterations. The Avizo™ 9 (ThermoFisher Scientific®) software was used to visualize the reconstructed volume.

Plasma Focused Ion Beam for Scanning Electron Microscopy (PFIB-

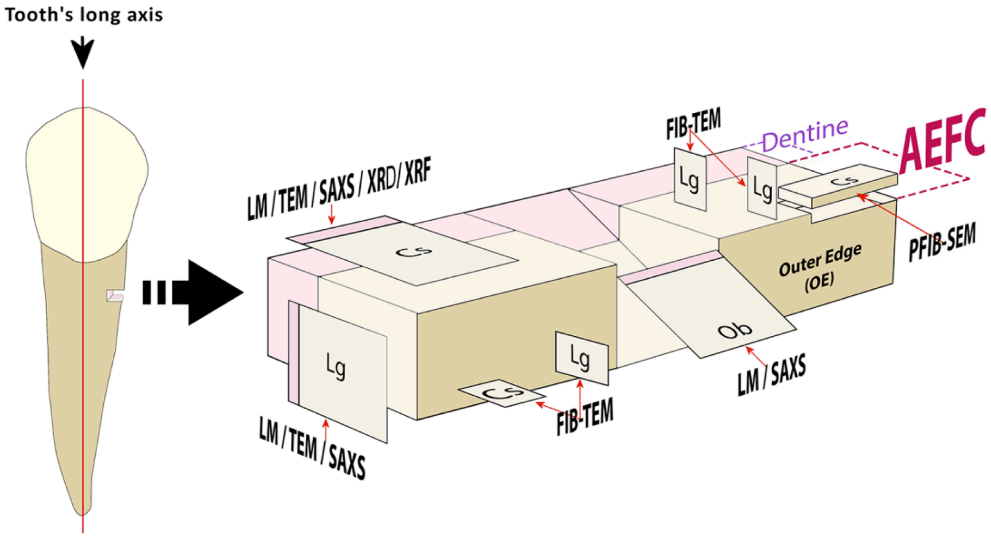

Fig. 2. Different cuts' orientations used according to the technique applied. Tooth's long axis taken as orientation reference for all (not drawn to scale). Abbreviations: Cs, *cross-section*; Lg, *longitudinal-section*; Ob, *oblique-section*; LM, *Light Microscopy*; TEM, *Transmission Electron Microscopy;* FIB-TEM, *Focused Ion Beam for Transmission Electron Microscopy*; PFIB-SEM, *Plasma Focused Ion Beam for Scanning Electron Microscopy*; SAXS, *Small-Angle X-ray Scattering*; XRD, *X-ray Diffraction*; XRF, *X-ray Fluorescence*; AEFC, *Acellular Extrinsic Fibre Cementum*.

***SEM) Tomography*.** Two sections were analyzed, one was demineralized and stained according to the OTOTO protocol, and the other was undemineralized. A Xenon-source PFIB microscope (Helios 5, PFIB UXe DualBeam, Thermo Scientific, USA) equipped with a Schottky field-emission gun SEM was used. The electron beam was focused on the exposed cross-section and imaging was completed with a retractable concentric backscattered detector (CBS). For the demineralized sample sequential milling and images were collected with a 0.80nA ion current and 2 keV accelerating voltage, while for the undemineralized sample milling was conducted at 4nA and imaging was performed with 3.5 keV and 3.2nA. For the demineralized sample, the first 20 slices were taken at 25 nm intervals without a rocking polish, then the subsequent slices thickness was of 50 nm and a 4° stage rocking angle was used to minimize curtaining artifacts (Loeber et al., 2017). For the undemineralized sample all slicing thickness was 25 nm with a rocking at 4 degree. Raw image data was aligned using SSD and Mutual Info in Dragonfly 4.1 (Objects Research Systems, Montreal, Quebec, Canada), followed by image smoothing (Chambo).

***Synchrotron scanning small-angle X-ray scattering (SAXS), X-ray Diffraction (XRD) and X-ray fluorescence (XRF)*.** Microbeam scanning experiments were performed on the 1 μm thickness sections mounted on the silicon nitride (Si_3N_4) membrane windows. Nine specimens were scanned using SAXS, three using XRD and five using XRF (Suppl. Mat. 3 Table S1), and a total scanned area dimensions (in most cases all cementum width along with a small area of the adjacent dentine were covered) (Suppl. Mat. 2 Figure S2). These three types of measurements were conducted in a sequential way at the Micro-focus Beamline ID13 of the European Synchrotron Radiation Facility (ESRF). The storage ring was operated in 7/8 + 1 multi-bunch mode with a maximum current of 200 mA. The primary X-ray beam was monochromatized to 13.6 keV, using a channel-cut Si (1 1 1) monochromator and focussed to a size of 2 (H) × 2 (V) μm^2 using a set of Beryllium compound refractive lenses (transfocator). For SAXS and XRD detection, an Eiger X 4 M pixel Detector (2070 × 2167 pixel, 75 × 75 μm^2 pixel size, DECTRIS Ltd., Baden-Daettwil, Switzerland) was used; while for XRF imaging, a Vortex-EM silicon drift X-ray detector (Hitachi, Japan) was employed (Suppl. Mat. 2 Figure S3). The sample to detector distance used for SAXS and XRD was of 978.06 mm and 145 mm, respectively, calibrated using a silver behenate standard along with the beam centre and detector tilt. In the case of XRF, the VORTEX detector was placed at 20 mm distance from the sample and was set to an angle of 45° (with respect to the incident beam) with the sample mounted perpendicular to the X-ray beam. Step sizes and exposure times used for all scans are in Suppl. Mat. 3 Table S2.

***SAXS data analysis*.** The two-dimensional scattering images were background subtracted and then azimuthally integrated to get one-dimensional scattering data by using the PyFAI library from ESRF (Ashiotis et al., 2015; Kieffer & Karkoulis, 2013; Kieffer & Wright, 2013). The principles of SAXS analysis have been described elsewhere (Fratzl et al., 1991, 1992, 1996; Gourrier et al., 2010, 2017; Pabisch et al., 2013; Wagermaier et al., 2013), and part of the information that can be extracted from this is related to the mineral particle dimensions as well as the predominant particle orientation (Pabisch et al., 2013). In this study, the correlation length between the mineral particles is considered as *T*-parameter (Gourrier et al., 2017) —instead of the average thickness that can be measured directly, under the assumption of a 50 % volume fraction of mineral phase (Fratzl et al., 1996)— (it was detected that the sample transmission data during the experiment were too noisy to normalize the SAXS measurements by the mineral density). In this way, according to the stack of cards model (Gourrier et al., 2010), the *T*-parameter (denoted in nm) provides an estimate of the average SAXS correlation length, which represents the particle thickness in first approximation (Gourrier et al., 2017). Regarding the predominant orientation of the mineral particles, this is described by the Rho-parameter which represents the fraction of oriented versus unoriented crystals (Pabisch et al., 2013; Wagermaier et al., 2013).

***XRD data analysis*.** The two-dimensional XRD patterns were analyzed using the software DPDAK v1.2.0 (Directly Programmable Data Analysis Kit;Benecke et al., 2014) to calculate *L*-parameter as previously reported (Lange et al., 2011). The *L*-parameter is defined as the average estimate of mineral particle length (under the assumption of a strongly crystalline material, which is assumed for mineralized tissues like bone), representing the mean domain size of the mineral platelets along the *c*-axis (Lange et al., 2011; Pabisch et al., 2013). Along the text we will refer to *L*-parameter as an estimation of the mineral particle length assuming all this latter. In this sense, each 2D XRD pattern, as an image, was integrated over the azimuthal angle (using the Fit2D integrator routine) and the radial intensities profiles were acquired for analysis and corrected for background. To visualize the distribution of *L*-parameter values, colour maps for each analysed sample were constructed by means of a Python code —written by the authors—, in which each μm^2 of the scanned area was assigned with its corresponding *L*-parameter value for the (0 0 2) Bragg reflection peak of the apatite crystals. On the other hand, to assess the preferred orientation of the apatite crystals, regarding the sample surface —considering that their *c*-axis is aligned with the collagen fibrils in parallel (Fratzl et al., 2004; McNally et al., 2012; Pabisch et al., 2013) (Suppl. Mat. 2 Figure S4a)—, three selected areas of 10 x 10 μm^2 were chosen by sample (outlined boxes in black dashed lines in Fig. 9a). For this purpose, an alignment parameter was created with CrystalDiffract 6.8.5 software (CrystalDiffract®, CrystalMaker Software Ltd, Oxford, England), to compare the integrated intensity of the (0 0 2) and (2 1 1) rings along with the domain size for the (0 0 2) *L*-parameter (Suppl. Mat. 2 Figure S5). Thus, diffractograms with different levels of preferred orientation of the *c*-axis were simulated to establish various values of this parameter: from 0 to 1, with 0 indicating that the apatite crystallites' *c*-axis are oriented haphazardly, *i.e.*, no preferred orientation (the integrated intensity of the (0 0 2) ring becomes weaker while the (2 1 1) increases and 1 that the apatite crystallites' *c*-axis has a closer alignment to the sample surface (the integrated intensity of the (0 0 2) ring is stronger than the (2 1 1) (Suppl. Mat. 2 Figure S4b-c). Following, these alignment parameter values were assigned to the each of the diffractograms (one by μm^2), acquired by the routine Peak Fit (Fit2D) in DPDAK, from the selected ROI's and distribution colour maps were created. Furthermore, the lattice parameters and its variations were calculated on selected areas of 20 x 20 μm^2 (400 pixels) along each of the cementum samples (outlined white boxes in Fig. 9a). To determine the cell dimensions of the crystal structure, *i.e.*, the lattice parameters *a* and *c*, the diffraction data were subject to a structural refinement analysis using the Rietveld method with the General Structure and Analysis Software II (GSAS-II) (Toby & von Dreele, 2013). Prior to running the Rietveld refinement, the crystallographic data for hydroxyapatite (Kay et al., 1964) was inserted into the input file, while silver behenate was used to calibrate the experimental control parameters. Likewise, the inner/outer parameter was set in the range of 14-21° in 2θ, in which the 002 reflection is located, and the background was modeled using Chebyshev polynomial with three coefficients to be refined. The statistical analysis for the assessed parameters, *L*- and alignment, were performed with IBM® SPSS® Statistics 21 software; the normality Kolmogorov-Smirnov test and non-parametric tests were used; alpha was set at $p < 0.05$.

***XRF data analysis*.** The fluorescence spectra were processed using the open source PyMCA (Python Multichannel Analyzer) software package (Solé et al., 2007). The fluorescence intensity of the elements of interest and their elemental distribution was obtained as 2D map.

3. Results and discussion

3.1. LM techniques

To corroborate that the samples from this study were taken from the type of tooth cementum of interest, the ~ 300 μm thickness sections where imaged with polarized and transmitted LM techniques. The main

features of the three different types of tooth cementum were observed as reported by e.g., Yamamoto et al., 2016: for AEFC the uniform incremental lines, for CIFC the irregular incremental lines with the embedded cementocytes, and for CMSC the combination of these two (Fig. 3a-c). The examination of the AEFC section of 150 μm thickness with differential interference contrast (DIC) technique, revealed mineralized Sharpey's fibres or collagen bundles (on a perpendicular position regarding the cementum's outer edge) branching out thinner fibres that are extended and oriented in parallel to the cemento-dentinal junction (Fig. 3g; Suppl. Mat. 2 Figure S6). These branched fibres, at this level of the AEFC's structure organization, seem well organized and could correspond to the incremental lines. The branching and anastomosing of

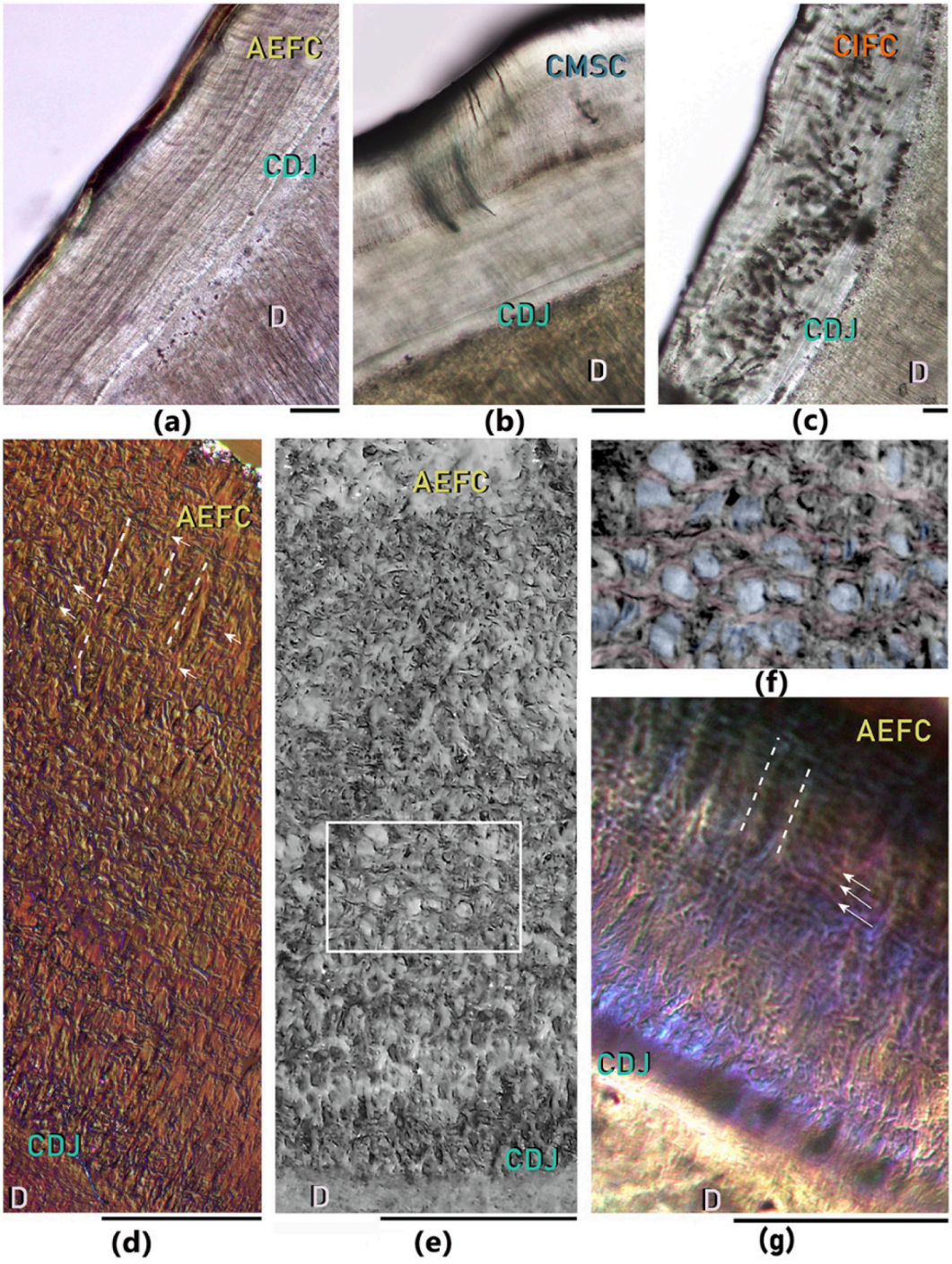

Fig. 3. Light microscopy images with different techniques. (a-c) Identification of three types of tooth cementum with transmitted light microscopy (sections of ~ 300 μm thickness), AEFC and CMSC in HATC-13 (a and b respectively), CIFC in HATC-26 (c). (d and g) Differential interference contrast images revealed the collagen alignment: smaller diameter mineralized collagen fibres are arrayed in parallel (white arrows), while thicker mineralized collagen bundles (discontinuous lines) are perpendicular to them (d, section of 1 μm thickness from HATC-05 and g, section of ~ 150 μm thickness from HATC-13). (e and f) Reflected light image of AEFC (section of 1 μm thickness) from HATC-05 (e) shows a clear area where collagen fibres are woven together by passing over collagen bundles (outlined white box magnified in f, where the smaller diameter fibres (reddish) and bundles (bluish) are slightly coloured to identify their perpendicular position to each other). All scales are 50 μm. Abbreviations: AEFC, *Acellular Extrinsic Fibre Cementum;* CMSC, *Cellular Mixed Stratified Cementum*; CIFC, *Cellular Intrinsic Fibre Cementum*; OE, *outer edge*; D, *dentine*; CDJ, *cemento-dentinal-junction*.

the mineralized Sharpey's fibres have been identified with TEM technique (Yamamoto et al., 2016) but without a relationship to the incremental lines. Hinrichs and collaborators (2022) identified some AEFC incremental lines with SEM concluding that these are formed by rich and poor density fibres. Contrary to this, the results by DIC in this research suggest that what the cited authors considered as rich density fibres possibly correspond to the aforementioned mineralized branched fibres, while the 'apparent spaces' between these latter might be what they named poor fibres. On the other hand, the visualization of the AEFC on 1 μm thickness section with DIC revealed the presence of parallel fibres on top of the mineralized Sharpey's fibres along the AEFC's width, however, a pattern similar to the incremental lines was not identified (Fig. 3d). Nonetheless, the observations with reflected light technique on 1 μm thickness sections of AEFC show that the mineralized collagen bundles and the branched fibres (oriented in parallel to the outer edge) are arranged similarly to a knitted fabric composite, comparable in a way to what has been reported for CIFC (Ho et al., 2009) (Fig. 3e-f).

3.2. TEM

The above mentioned observations about the branching and anastomosing of the Sharpey's fibres were confirmed with TEM. It was observed with TEM micrographs of 250 nm thickness sections that some areas of the Sharpey's fibres were covered (totally or in parts) by the branched fibres, having a clear orientation in parallel to the outer edge of the cementum (Suppl. Mat. 2 Figure S7); while with a 200 nm thickness sections, it was noticed that such branched fibres were placed with oblique, curvy and transversal orientations (Suppl. Mat. 2 Figure S8). Furthermore, with the 175 nm thickness sections, it could be observed that some of the branched fibres are displayed, following a semicircular and arched direction, on top of the Sharpey's fibres (Suppl. Mat. 2 Figure S9). Likewise, with the 150 nm thickness sections, it was

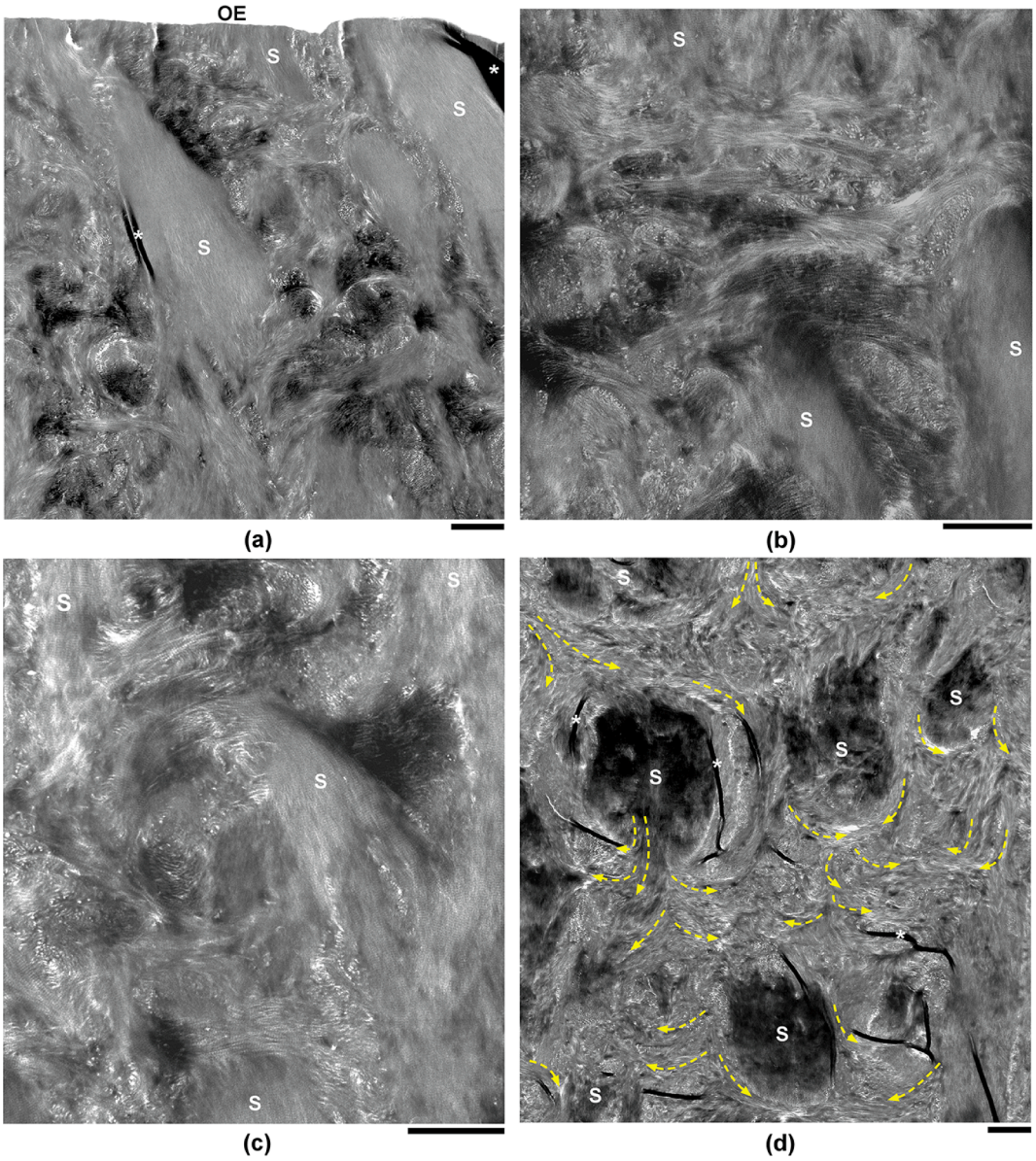

Fig. 4. TEM images from the ultramicrotomed section. (a-c) HATC-13 cross-sections (150 nm thickness) show the perpendicular position of the Sharpey's fibres (S) relative to the outer edge (OE) of AEFC (a) and how these branch out to form transversal collagen fibres which interconnect among themselves (a-c). (d) On a thinner cross-section (90 nm thickness) the spaces left by the Sharpey's fibres (which were cut by the ultramicrotome) are noticeable (labelled with S) as are the curvy directions (yellow arrows) that the fibres take to become interconnected. Asterisks point to fine folds. All scale bars are 2 μm. (For interpretation of the references to colour in this figure legend, the reader is referred to the web version of this article.)

identified that the branched fibres appear not to be extended or remain at the same level of the Sharpey's fibre that they come from (Suppl. Mat. 2 Figure S10); this means that, such Sharpey's fibres ramifications can take diverted orientations at different levels of the AEFC, and that is why there are fibres oriented on the three planes of the space (Fig. 4a-c; Suppl. Mat. 2 Figures S10 and S11). In this sense, it was observed that the starting point of the mineralized Sharpey's fibres is not always seen at the outer edge of the cementum but protruding at any position along the AEFC's width (Fig. 4a-c and, as explained later for Fig. 7b). This latter was clearly observed on a thinner section, 90 nm thickness, because the mineralized branched collagen fibres tend to follow a curvy direction surrounding the mineralized collagen bundles (Fig. 4d). On the other hand, the HATC-12 sample that was prepared according to the OTOTO protocol, shows the already mentioned complex features of the Sharpey's fibres; and because this sample was demineralized, it can be observed the diminishing of firmness of the structure (Suppl. Mat. 2 Figure S12).

The samples that were prepared with FIB for TEM, on a smaller scale, confirmed the different orientations of the mineralized collagen fibres along the width of the AEFC on the *X*,*Y* and *Z* planes (Fig. 5). In this sense, the full tilt-series that was collected for the HATC-13 sample for electron tomography (Fig. 5a), clearly show the branching out of the fibres as well as the perpendicular position (*Z* plane) of the fibres. This latter is noticed with the circular black 'holes', which correspond to the ~ 50 nm diameter collagen fibrils that are surrounded by stacks of mineral lamellae (Grandfield et al., 2018; Schwarcz et al., 2020) (Suppl. Mat. Video 1; Fig. 5d-e). Therefore, as expected, the *c*-axis of the apatite crystals was seen to be in parallel to the collagen fibres when these were positioned on the plane X-Y but not when they were on the *Z* plane (Suppl. Mat. 2 Figure S14).

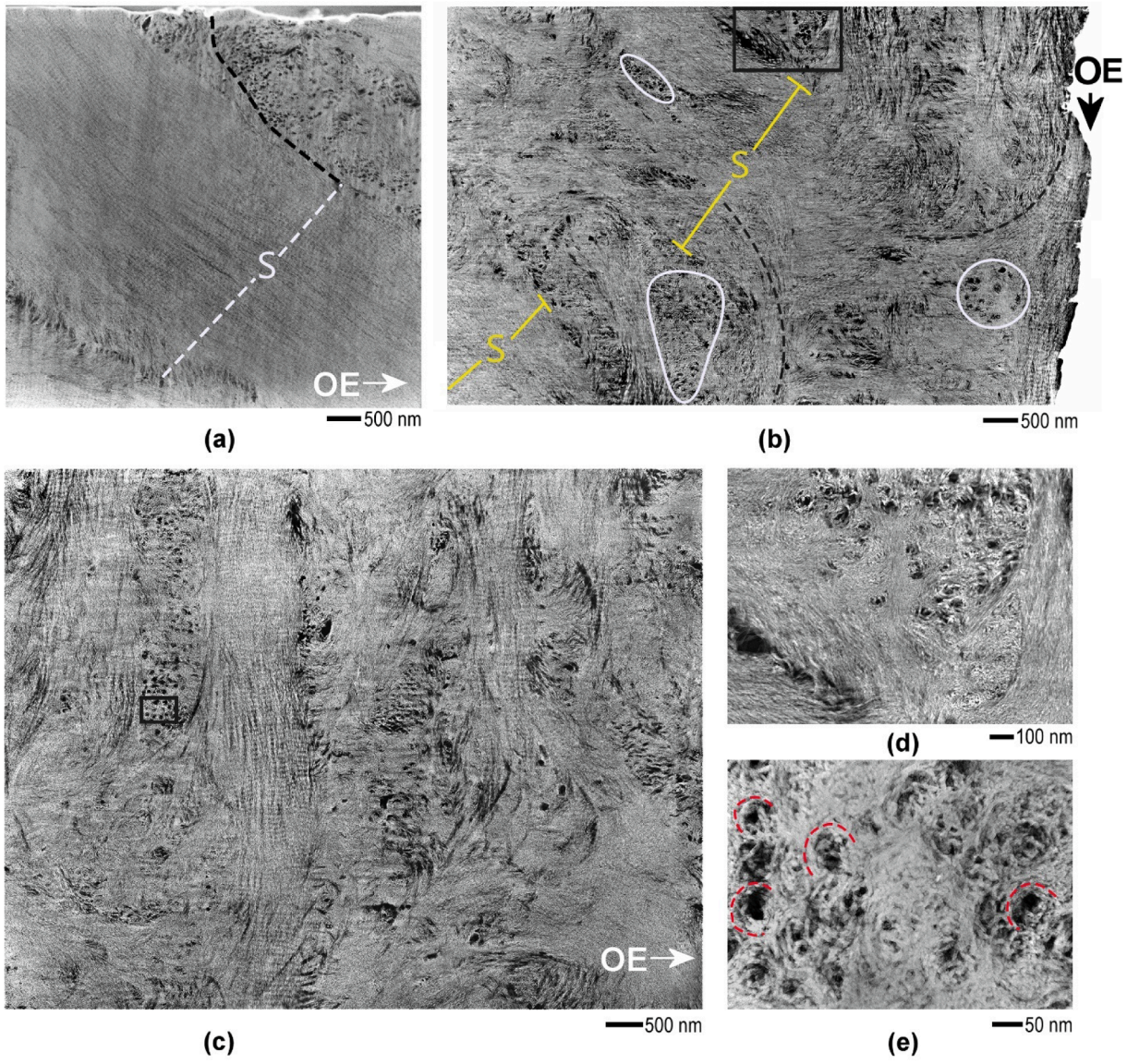

Fig. 5. STEM images of FIB sections. (a and b are longitudinal cuts, while c is a cross-section; see Fig. 2). (a) A Sharpey's fibre (S) of about 4.5 μm width is positioned diagonally towards the outer edge (OE) of AEFC, having a thin section of its upper side branching out (black dashed line) among the adjacent collagen fibres that are set in the perpendicular or Z direction (as coming out of the surface) (see Suppl. Mat. Video 1). (b) The branched mineralized collagen fibres follow mainly curvy directions (black dashed lines; see Suppl. Mat. 2 Figure S13); furthermore, there are fibres projected on a Z direction (examples are outlined in white circumferences), which are similar as the magnified image in e). (c) Some of the branched mineralized collagen bundles of different width (about 1.4 μm and less) are positioned in parallel to the OE of AEFC among other collagen fibres that are displayed diagonally and perpendicularly. HAADF-STEM images: (d) section showing the layout of the different directions that the mineralized collagen fibres can take (outlined black box in b). (e) Higher magnification of a group of mineralized collagen fibrils on a Z direction (outlined black box in c) surrounded by mineral lamellae, which form curvatures structures around each fibril (outlined in red dashed lines).

3.3. PFIB-SEM

The first PFIB-SEM was conducted on one section of the HATC-12 sample, which was demineralized and stained with osmium tetroxide (OTOTO protocol). The dimensions of each of the 73 slices produced and acquired with PFIB-SEM were about 70 μm x 49 μm (Suppl. Mat. 2 Figure S15), marginally greater than the half of the complete AEFC's width for the sample HATC-12. In most of the PFIB-SEM images some AEFC structures were obscured by the presence of curtaining, an artifact caused by the electron beam; consequently, before the procedure of alignment and reconstruction, a de-striping algorithm was applied to each half of the dataset to diminish the presence of the artifact. However, despite this latter interference, the whole reconstructed volume had to be cropped, selecting the areas where the AEFC structure's transitions were better visualized. In this sense, the measuring of the resulting 2D reconstruction was about 48 μm X 35 μm (Suppl. Mat. Video 2), while two 3D reconstructions were obtained, the first about 50 μm x 35 μm X 4 μm^3 (Suppl. Mat. Video 3) and the second, 20 μm x 23 μm X 4 μm^3 (Suppl. Mat. Video 4; see the outlines boxes in Suppl. Mat. 2 Figure S15). It can be seen that the Sharpey's fibres predominant

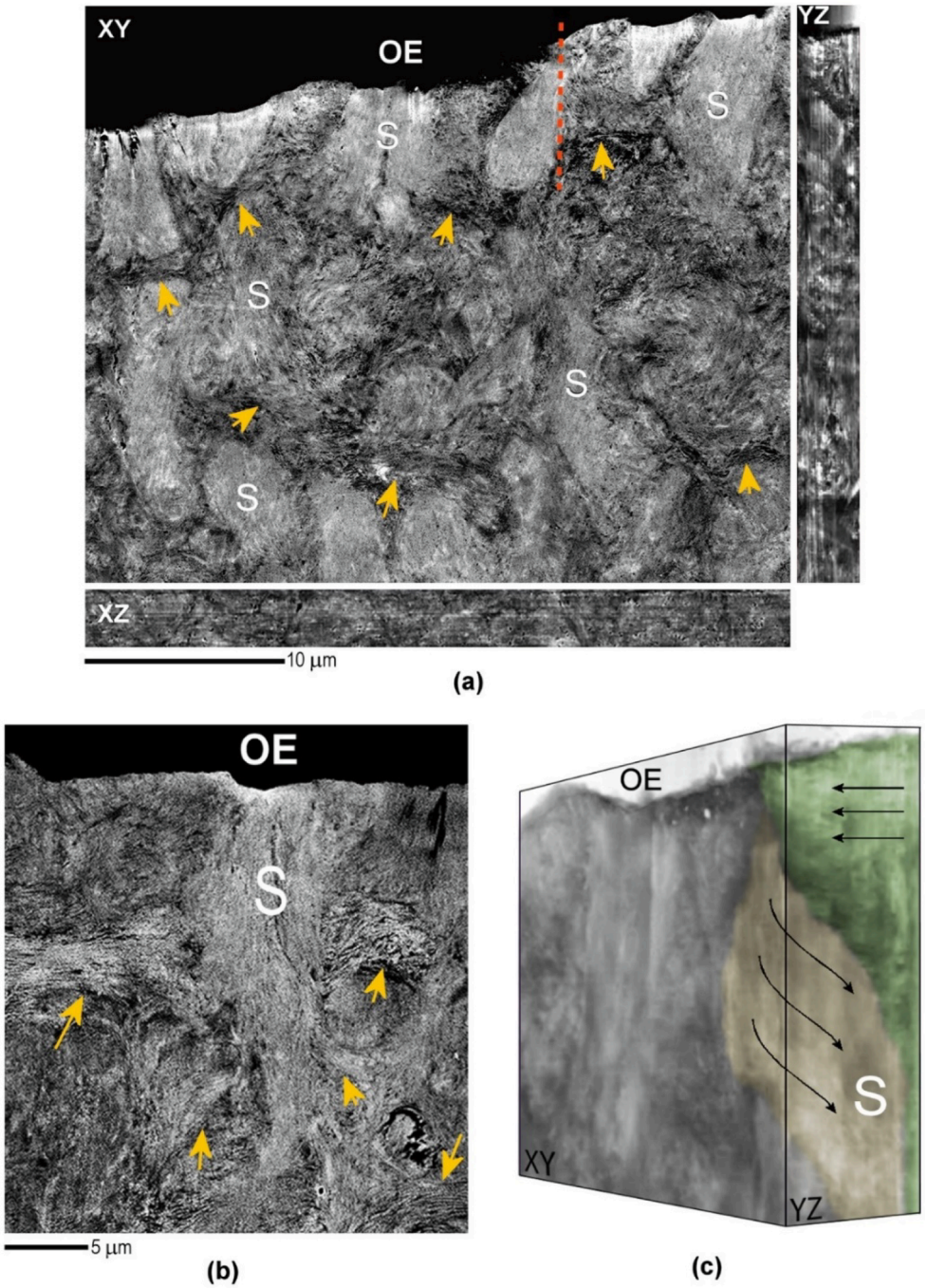

Fig. 6. PFIB-SEM of demineralized AEFC. Images extracted from the XY, XZ and YZ planes of the reconstructed volume (see Suppl. Mat. 2 Figure S15): a) The predominant perpendicular position of the Sharpey's fibres (S) regarding AEFC's outer edge (OE) and, among them the branched collagen fibres display a different orientation (yellow arrows). b) An example of the branched collagen fibres (yellow arrows) coming out from a Sharpey's fibre. c) ROI from the 3D reconstruction (Suppl. Mat. Video 4) the parallel direction of the branched fibres (coloured in green) in the way to cover the Sharpey's fibre, which has an oblique orientation (see the red dashed line in (a) for the YZ location).

orientation is perpendicular towards the AEFC outer edge, while the fibres that branched out from them take a different orientation; these branched fibres are placed among and on top of the Sharpey's fibres (Fig. 6a-b; Suppl. Mat. Video 2). The PFIB-SEM reconstructions allowed us to see that the flow of the Sharpey's fibres is always interrupted by the branched fibres, which wrapped some of their segments in a progressive way and in sequence but not all at the same time, *i.e.*, when one segment is covered another is uncovered, successively (Suppl. Mat. Video 3). Furthermore, the YZ plane show how the branched fibres (set in parallel to the AEFC outer edge) cover progressively a Sharpey's fibre following a curvy direction (Fig. 6c; Suppl. Mat. 2 Figure S16 and Suppl. Mat. Video 4). Besides, it can be seen that the branched fibres placed at the lateral sides of a Sharpey's fibre are joined on top of this latter to form a collagen bundle following a semicircular and arched direction, as it was observed on the TEM images (Suppl. Mat. 2 Figures S9 and S16). The visualization of the branched fibres on the YZ plane explains why some of the sections prepared for TEM show circular 'black holes' which correspond to the collagen fibres positioned on the Z plane. Also, it is important to note that the branched fibres on the XY plane are seen in different positions according to the Z plane change.

The second PFIB-SEM was done on one section of the HATC-13 sample, which was undemineralized. Data were processed (907 images were aligned, cropped and denoised) in order to get to the final volume that was about 30 μm width x 33 μm height x 23 μm depth (the height dimension covered about a third of the complete AEFC's width of HATC-13 sample) with a voxel size of 25 nm (Fig. 7a). During the acquisition process the SEM fiducial marker shifted, which led to defocus around processed data slice 795; which explains the discontinuity at around 20 μm into the volume. As it can be appreciated in the reconstructed volume, the charging effect (bright flashing detected mainly on the XY plane; Suppl. Mat. Video 5) was caused due to this mineralized tissue having a porous structure. The voltage used allowed us to see sufficient compositional contrast.

In this sense, the reconstruction from the XY plane (Suppl. Mat. Video 5) show Sharpey's fibres, oriented perpendicular to the AEFC outer edge, branching out fibres that constantly cover and uncover other collagen bundles following a curvy direction. Besides, the dimension of this reconstructed volume allows to see that these branched fibres form

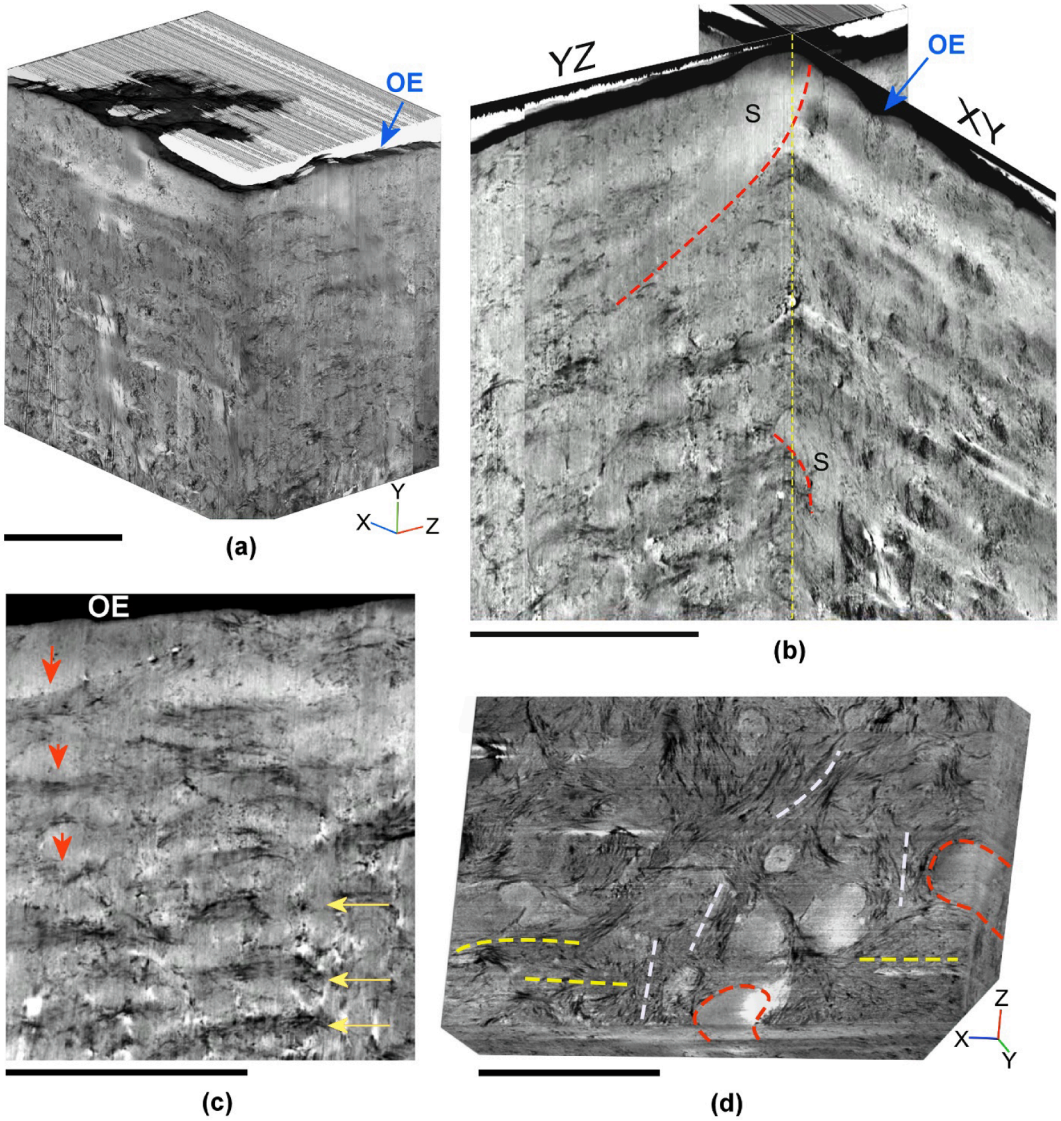

Fig. 7. PFIB-SEM of undemineralized AEFC. (a) Reconstructed volume. (b) Outlined (red dashed lines) are examples of Sharpey's fibres (S) displayed in two orthogonal planes (see Suppl. Mat. Video 7). (c) Regarding AEFC outer edge (OE) the parallel fibres (yellow arrows), formed by the branched fibres, are clearly seen on the YZ plane and, among them, are sections of the Sharpey's fibres with a perpendicular direction (red arrows) (Suppl. Mat. Video 6). (d) From the XZ plane, an interweaving of the branched fibres are denoted with some of their sections oriented towards the X and Z axis (yellow and white dashed lines respectively) (Suppl. Mat. Video 8). All scales are 10 μm. (For interpretation of the references to colour in this figure legend, the reader is referred to the web version of this article.)

arched structures aligned (as seen with more detail with TEM, Suppl. Mat. 2 Figure S9). Subsequently, these arched structures are joined to each other at their upper zone by the same branched fibres, which at this point have taken a parallel direction towards the AEFC outer edge (Fig. 7c). In this sense, the view from the YZ plane clearly show the presence of these parallel fibres all the way through the X direction (Suppl. Mat. Video 6). Furthermore, among these parallel fibers, sections of the Sharpey's fibres can be seen oriented in a perpendicular direction, towards the outer edge (Fig. 7c). The visualization of the two orthogonal planes show that the Sharpey's fibres are lay out crossing both planes (Fig. 7b; Suppl. Mat. Video 7), which confirmed the observations made in this research with TEM when referring to the Z-axis. While from the AEFC outer edge view, or XZ plane, it can be appreciated an interweave of the branched fibres following mainly circular directions with some of their sections oriented towards the X and Z axis, which produce the mentioned parallel fibres seen from the other planes (Fig. 7d; Suppl. Mat. Video 8). These results are consistent with the findings on the demineralized sample with this same technique.

One of the advantages of using sectioning techniques such as FIB and PFIB is the maintenance of ultrastructural features that, otherwise they could be lost, totally or in part during the sectioning process with ultramicrotomy (Binkley et al., 2020; Grandfield et al., 2018; Jantou et al., 2009). Also, when this latter sectioning technique is used, the thickness of the sample must be considered, because in this work it has been demonstrated that fewer features were observed when slices of 90 nm thickness were employed for TEM. This could explain why in the TEM images published elsewhere (e.g., Yamamoto et al., 2016) the curvy and lateral fibres, are not present or not so obvious.

The PFIB-SEM along with the LM and TEM results clearly demonstrate that the complex organization of the Sharpey's fibres led to display constant and continuous parallel fibres regarding the AEFC outer edge, which is in accordance with recent research (Colard et al., 2016; Aboulfadl and Hulliger, 2008). Decades ago, such parallel fibres were identified by Furseth (1974), who opened the possibility that these were 'intrinsic fibres', but years later this hypothesis about their origin and its presence in the AEFC was dismissed (Bosshardt & Schroeder, 1991). The results presented here conclusively show and confirm what Kvam (1973) suspected, and Raspanti and collaborators (2000) suggested, that the so-called lateral fibres come from the same Sharpey's fibres, which bend and branch consistently. Now, we also know that a branched fibre form an arched structure that will be joined to the next by these same fibres but in a parallel fashion and, consequently, the length of the parallel fibres would be corresponding to the length of such aligned arched structures.

With the PFIB-SEM results we were able to see that AEFC is a complex mineralized tissue that is not organized by uniformed layers. On the contrary, the Sharpey's fibres before branching out are laid out, not only on one orthogonal plane but crossing along two (as seen in Fig. 7b). Opposing this it seems that the aligned arched structures formed by the branched fibres are laid out according to each of XY and YZ planes. Therefore, when all branched parallel fibres are together and superimposed in a block of 150 μm, these would be projected as the AEFC incremental lines if observed with polarized LM. This latter is due to the collagen birefringence (Stutz, 2002) as if the parallel fibres were part of a continuum, but they are not. Also, because the arched structures, and consequently the parallel fibres, are laid out in both orthogonal planes *i.e.*, XY and YZ, the AEFC incremental lines with polarized LM can be seen in both mentioned planes. On the other hand, the bright and dark alternating pattern, characteristic of the AEFC incremental lines, can be clearly associated with the different fibres' orientations, *i. e.*, among the parallel fibres are sections of Sharpey's fibres running perpendicularly to them (Fig. 7c). This is similar, in principle, to the incremental pattern found in elephant tusk dentine (ivory), where the dark bands are due to tubules oblique to the surface, while the bright ones are associated with tubules parallel to it (Albéric et al., 2017).

Undoubtedly, more focussed research is needed to better understand the role of the arched structures formed by the branched fibres that come from the Sharpe'y fibres, to see if somehow there is a relationship with the distribution of loads and forces that are exerted on this mineralized tissue, considering that AEFC is crucial for tooth attachment (Bosshardt, 2005). Furthermore, we can suggest that the complex display of the collagen fibres depicted in the PFIB-SEM images, is probably the extension of the PDL's collagen fibres meshwork (de Jong et al., 2017; Hirashima et al., 2019; Hirashima et al., 2020b; McCulloch et al., 2000; Raspanti et al., 2000; Yamamoto et al., 2016). In this sense, the organization, orientation and all arrangements of the AEFC's collagen fibres must be set at the interface with the PDL, where the mineralization front takes place (Bosshardt & Schroeder, 1991; Raspanti et al., 2000).

3.4. SAXS and XRD

With SAXS it was possible to identify the predominant orientation of the mineralized collagen fibres in all measured samples. For AEFC, on cross-cut sections, the orientation was mainly perpendicular to its outer edge, in some cases following a straight direction and in others obliquely (Suppl. Mat. 2 Figure S17a, d-f), while fibres with parallel orientation, or close, were not so remarkable except for the upper area of HATC-27 (Fig. 8a). It is highly possible that the irregular and lesser presence of the fibres with lateral orientation is due to the ultramicrotomy sectioning technique used, which, as mentioned earlier, can cause the loss of some structural features. In the case of the longitudinal section of AEFC (Suppl. Mat. 2 Figure S17b), the perpendicular orientation of the fibres, mainly with a straight direction, were predominant, while for the oblique section (Suppl. Mat. 2 Figure S17c) all orientations were seen.

These results are in accordance with the observations made with TEM and PFIB-SEM, as well as the black spaces among fibres, which correspond to fibres situated on the Z plane. On the other hand, for the other two types of tooth cementum —scanned for comparison—, the mineralized fibres of *cellular intrinsic fibre cementum* (CIFC) sample (Fig. 8c) show a mixture of all orientations but predominantly oblique and parallel. This experiment revealed that this CIFC sample is of the type 'extrinsic fibre-poor', that is why some fibres have a perpendicular orientation. Whereas the *cellular mixed stratified cementum* (CMSC) sample (Fig. 8b) displays a clear difference between the two areas scanned, the top one with the fibres oriented in a similar fashion, is trending to a lateral orientation (which demonstrate that this CIFC is 'extrinsic fibre-free'), while the bottom area show a mixture of all orientations, similar to AEFC; which makes sense considering that CMSC it is composed by CIFC and AEFC (Yamamoto, et al., 2016).

Regarding the T-parameter, understood as the correlation length between the plate-shaped mineral nanocrystals, it was quantified from the radially integrated patterns resulting from all SAXS measurements. Therefore, in all samples it was found that the T-parameter value was relatively homogeneous (changing with the depth in the samples), having an estimated average value ranging from 3 to 3.7 nm (Figures 8 and Suppl. Mat. 2 S2 Figure S17). Furthermore, a clear offset and relatively sharp transition between cementum and dentine was noticeable, with a slight increase of the T-parameter estimated average values ranging from 4 to 4.7 nm. Even though, the T-parameter value in this research is considered to represent the particle thickness in first approximation, these results are not too distant to what has been reported for other mineralized tissues when T-parameter is considered as the average thickness of the crystals (under the assumption that variations in the mineral volume fraction are minor), for example bone is around 3.5 nm (Casanova et al., 2023; Fratzl et al., 1992; Fratzl-Zelman et al., 2014; Roschger et al., 2001; Xi et al., 2021), and crown dentine depending on its location can range from 2 to about 3.5 nm (Märten et al., 2010). Moreover, considering that for dentine it has been observed that there is a trend of T-parameter value to increase with age (Akabane et al., 2021), here this was not the case for most of the samples, which corresponding age is up to the fifth decade of life (see Table 1). However, the sample HATC-05 which individual's age was of 92 years shows,

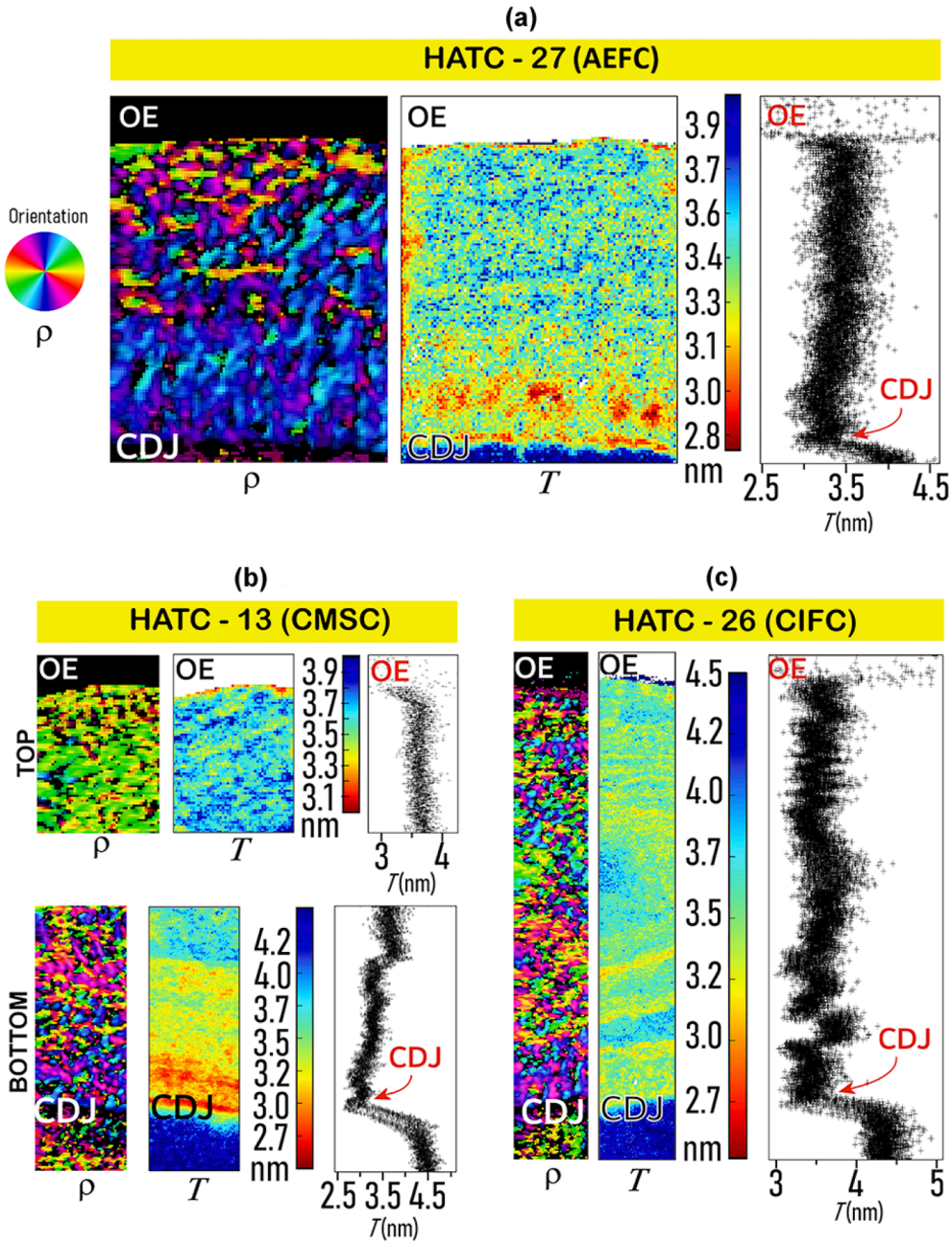

Fig. 8. SAXS results. For each sample, the colour map on the left is illustrating the orientation and scattering intensity of the mineralized collagen fibres (ρ, Rho parameter), which are colour-coded according to the wheel on the left; while in the middle, it shows the mapping of the resulting *T* parameter (the correlation length between particles in nm), with its corresponding colour scale bar; and, on the right is plotting the distribution of *T* parameter values along the sample. (a) Cross-section of Acellular Extrinsic Fibre Cementum (AEFC). (b) Cross-section of Celullar Mixed Stratified Cementum (CMSC). (c) Cross-section of Cellular Intrinsic Fibre Cementum (CIFC). See Suppl. Mat. 2 Figure S2 for the information about the samples and the scanning areas and, Suppl. Mat. 2 Figure S17 for the SAXS results for the other six AEFC samples. Abbreviations: OE, *outer edge*; CDJ, *cemento-dentinal junction.*

slightly, the greatest T-parameter values; for sure further research will be needed to assess if mineral changes, associated with ageing, take place in tooth cementum.

The *L*-parameter sequential adjustment with Fit2D was done successfully for most of the data from the three scanned samples (HATC-65, HATC-27 and HATC-05). For the cases when the adjustment with Fit2D failed (because it was producing negative, significantly high or unreasonable values) it is reasonable to consider that the cause was related to the sample's structure. This means that, the measurements that produced incorrect fittings took place at the spots where the mineralized collagen fibres were oriented on the *Z* plane (see Fig. 5), where from the observer plane, the HAp (002) reflection, used for L-parameter calculation, is absent (see Suppl. Mat. 2 Figure S14). In this sense, along each of the samples the percentage of the data that could not be used to calculate L-parameter was 19.12 % for HATC-65, 12.67 % for HATC-27 and 8.82 % for HATC-05. Therefore, data sets were filtered from the values originated by an incorrect adjustment with Fit2D and then, the Kolmogorov-Smirnov test showed that all analyzed data sets were not distributed normally ($p < 0.05$).

In Fig. 9a the mappings of L-parameter values for AEFC are presented, having an average of 19.17 nm (sd = 2.20) for HATC-65, 18.31 nm (sd = 1.24) for HATC-27, and 19.71 nm (sd = 1.92) for HATC-05. Whereas, for dentine a clear difference of L-parameter was noticed (similarly to what it was seen for T-parameter), 23.59 nm (sd = 0.48) for

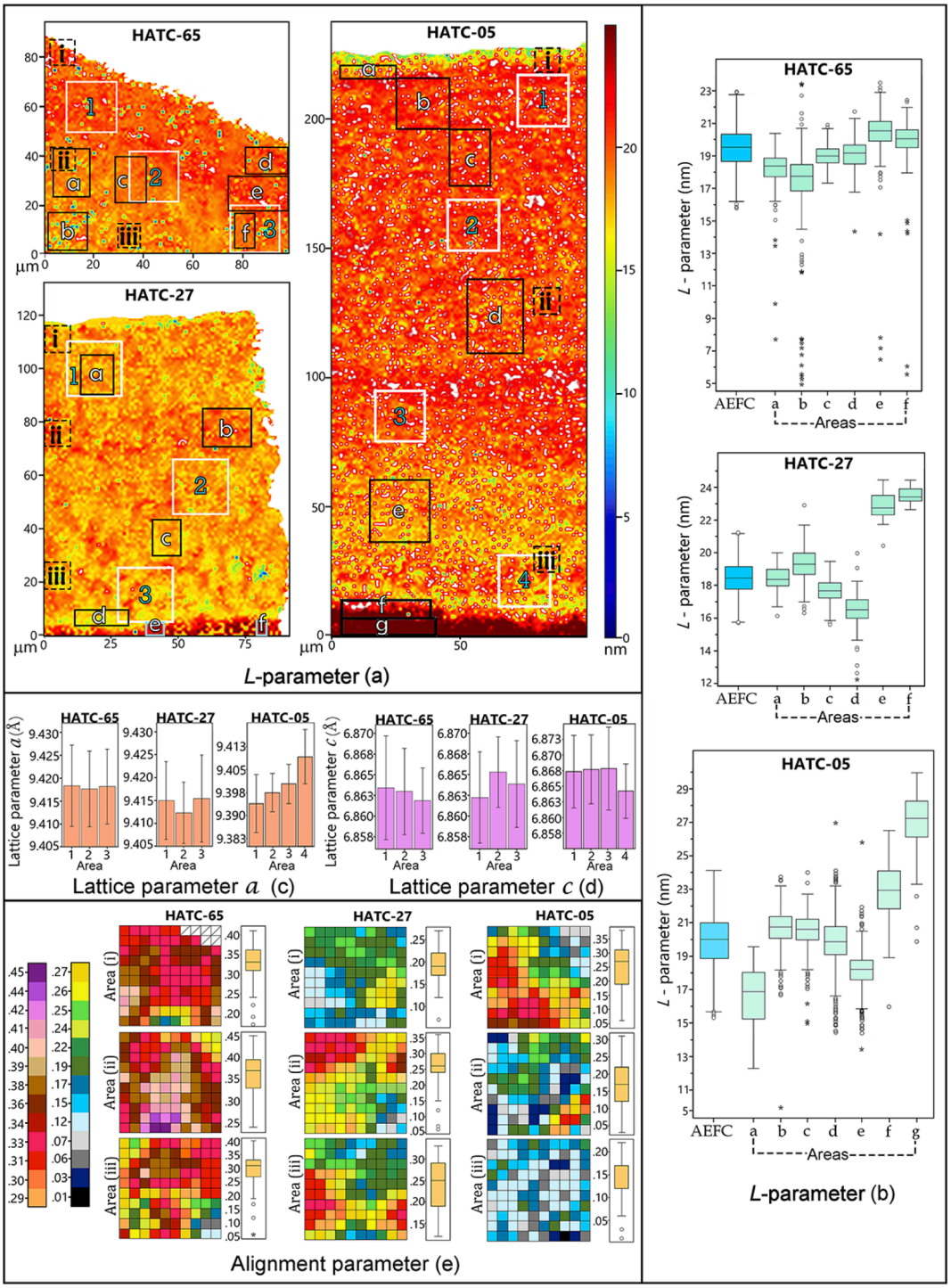

Fig. 9. XRD results. (a) Colour mappings of L-parameter values (nm) for the three scanned samples with its corresponding colour scale bar (see Fig. 3 for the information about the samples and scanning areas). (b) L-parameter values distribution for the complete AEFC as well as for the selected areas along each sample (outlined black boxes in a). (c and d) Values of lattice parameter a and c for selected areas (outlined white boxes in a). (e) Mappings of the alignment parameter values for the selected areas (outlined boxes in black dashed lines in a) are in colour-coded according to the colour scale bars and its distribution are shown in the corresponding boxplots.

HATC-27 (areas e and f in Fig. 9b) and 27.35 nm (sd = 1.82) for HATC-05 (areas f and g in Fig. 9b); however, for HATC-65 an offset with dentine was not clear probably because of the small scanned area for this latter (see Suppl. Mat. 2 Figure S2).

The distribution of L-parameter values along each of the samples can be seen in Fig. 9b, according to the selected areas (outlined black boxes in Fig. 9a). To compare the distribution of *L*-parameter values of the three samples, the data without the CDJ and dentine values were cleaned from the extreme values (Suppl. Mat. 3 Table S3). Thus, it was observed that the difference between the maximum and minimum values was major for HATC-05 (Suppl. Mat. 2 Figure S18). In addition, the Kruskal-Wallis test showed that there were significant differences between the three analyzed samples ($p < 0.5$), and the Games-Howell post-hoc test identified that such difference existed among each of

them ($p < 0.05$ for each compared pair). With respect to the age of the individuals to whom the samples belong, a relationship with L-parameter was not seen. For example, the sample HATC-65 came from a 20-year-old individual and HATC-05 from a 92-year-old, both presenting a minimum difference between their means L-parameter, having 19.49 nm and 19.86 nm, respectively; while HATC-27 came from a person of 55 years and showed a mean value of 18.37 nm. Therefore, it can be assumed that, in general, with the mineralization process L-parameter, as an estimation of the mineral particle length, of the produced apatite crystallites in the AEFC are within an average range of 18 and 19 nm irrespective of the individual's age.

It is important to mention that the absolute values obtained here, for L-parameter, are probably an underestimation of the actual crystal size. The existing knowledge about the apatite crystals dimensions in tooth cementum is limited and this has been obtained fundamentally by TEM observations. For example, Selvig (Selvig, 1965) reported that in the calcification front of acellular and cellular cementum, the apatite crystals did not measure more than 40 nm in length, 20 nm in width and of 2 nm in thickness. While within a few microns away from the calcification front, the crystals already 'matured' increase their dimensions showing a fairly constant thickness of about 8 nm, but with wider variations in the length and width. According to this latter, Bosshardt and Selvig (Bosshardt & Selvig, 1997) reported also greater variation in length and width among the crystals in deep layers of cementum. Furthermore, elsewhere it has been reported, but without stating the source of the technique (Berkovitz et al., 2018; Duailibi et al., 2006) that cementum apatite crystals measure about 55 nm of width and 8 nm of thickness. To our knowledge, this is the first study with an approach to estimate the apatite crystals' dimensions in the AEFC mineralized tissue in great detail, under the assumptions that L-parameter is a typical estimate of mineral particle length (assuming that tooth cementum is a strong crystalline material such as bone) and T-parameter as the average correlation length, representing the particle thickness in first approximation.

Regarding the alignment parameter, it was found that in all selected areas within each of the three samples (outlined boxes in black dashed lines in Fig. 9a) the resultant values ranged from 0.01 to 0.45 (Fig. 9e and Fig. 10), which means that, towards the sample surface, the crystallites' *c*-axis are from being partially aligned to be haphazardly oriented (see Suppl. Mat. 2 Figure S4c and Figure S5). Understanding that the *c*-axes of the apatite crystals are generally aligned in a parallel way, to the long axes of the collagen fibrils (McNally et al., 2012), these results are in accordance with our observations on the TEM images, mentioned earlier, where it was found that the mineralized collagen fibres can take different orientations in one same place. Also, this agrees with the predominant complex organization of the collagen fibrillar architecture, which has been visualized like a meshwork of interwoven collagen bundles and fibrils in AEFC (de Jong et al., 2017; Hirashima et al., 2020b; McCulloch et al., 2000; Raspanti et al., 2000; Yamamoto et al., 2016).

On the other hand, the calculated values for lattice parameter *a* and c were carried out successfully on the selected areas for each sample (outlined white boxes in Fig. 9a; Table 2). The values for lattice parameter *a* were relatively closer to the published values for bone and dentine, but lower than enamel, whereas our results for lattice parameter *c* were lower than what is has been reported for other mineralized tissues (Table 3).

The performance of lattice parameter *a* within the selected areas in HATC-65 and HATC-27 is consistent, but the opposite is seen for HATC-05, which values were the lowest and changed progressively along the cementum width (Fig. 9c). Furthermore, the values of lattice parameter *a* vary in each of the measured points (by row and by column within the selected areas, as seen in Suppl. Mat. 2 Figure S19); in this study a pattern of the increase/decrease of such values that could be related to the AEFC incremental lines was not found, as it has been indicated for other species (Ryan et al., 2020). Among the areas from each of the samples, the values of lattice parameter *c* were similar, nonetheless HATC-05 show slightly higher values (Fig. 9d). Both lattice parameters, *a* and *c*, presented noticeable differences for HATC-05 (Suppl. Mat. 2 Figure S20), which came from an individual of 92 years old, that could be as a result of changes in the chemical composition of the apatite due to ionic substitutions, such as Na, Mg, Cl, or F, and variations in the

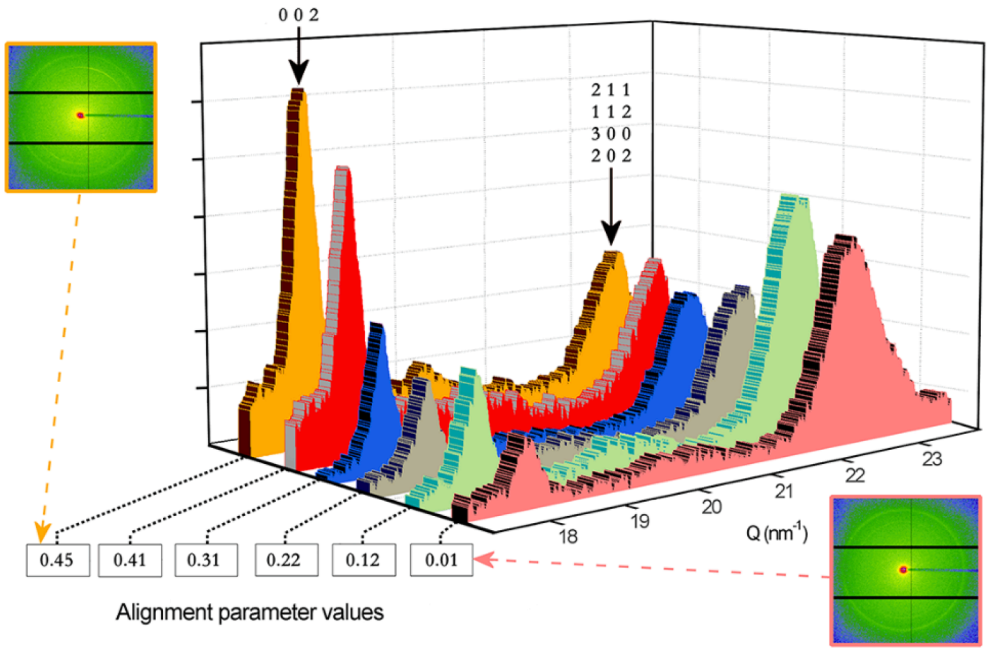

Fig. 10. Range of the alignment parameter values found in the analyzed selected areas (outlined boxes in black dashed lines in Fig. 9a). The 002 reflection is at Q = 18.26 nm^{-1}; while the 211, 112, 300 and 202 reflections are located at Q = 22.31, 22.61, 23.08 and 23.88 nm^{-1} respectively and are strongly overlapped. The values of the alignment parameter vary from 0 to 1 (see text for explanation). The diffraction ring corresponding to the highest found alignment parameter value is similar to the representation of the 002 planes in Suppl. Mat. 2 Figure S5a, while the ring corresponding to the lowest alignment parameter value is as shown in Suppl. Mat. 2 Figure S5b (see Suppl. Mat. 2 Figure S4).

Table 2
Resulted lattice (*a* and *c*) parameter values.

	HATC 65		HATC 27		HATC 05	
	Lattice parameter		Lattice parameter		Lattice parameter	
	a-Axis (Å)	*c*-Axis (Å)	*a*-Axis (Å)	*c*-Axis (Å)	*a*-Axis (Å)	*c*-Axis (Å)
Area 1	9.4183(4)	6.8634(1)	9.4149(4)	6.8622(1)	9.3938 (4)	6.8673 (1)
Area 2	9.4176(5)	6.8629(1)	9.4122(4)	6.8653(1)	9.3974 (4)	6.8676 (1)
Area 3	9.4181(6)	6.8618(1)	9.4154(4)	6.8638(1)	9.4002 (4)	6.8678 (1)
Area 4					9.4091 (4)	6.8642 (1)
All areas	9.4180(5)	6.8627(1)	9.4142(4)	6.8638(1)	9.4001 (4)	6.8667 (1)

*Standard uncertainty is in parenthesis.

Table 3
Published lattice parameter values (*a* and *c*).

	Lattice parameter		Reference
	a-Axis (Å)	*c*-Axis (Å)	
Enamel	9.441(2)	6.878(1)	(Wilson et al., 1999)
	9.4660(9)	6.901(3)	(Al-Jawad et al., 2007)
	9.441	6.880	Reviewed by (Kannan et al., 2008)
Decidual enamel	9.44	6.88	(Kallaste & Nemliher, 2005)
Dentine	9.430(2)	6.883(3)	(Kallaste & Nemliher, 2005)
	9.421	6.887	Reviewed by (Kannan et al., 2008)
Bone	9.4354 (33)	6.8866(4)	(Foley et al., 2020)
	9.41	6.89	Reviewed by (Kannan et al., 2008)
HA	9.432	6.881	(Kay et al., 1964)
	9.4176	6.8814	(Elliot, 1994)
	9.421	6.884	Reviewed by (Ratnayake et al., 2017)
	9.430	6.891	Reviewed by (Kannan et al., 2008)
OHAp	9.4243 (55)	6.8856 (35)	(Morgan et al., 2000)

carbonate content as well as the Ca/P ratio (Al-Jawad et al., 2007; Ratnayake et al., 2017). Besides, considering that AEFC grows by apposition and does not experience turnover and remodeling like bone (Bilgin et al., 2004; Bosshardt & Sculean, 2009), the direction of the reduction of lattice parameter *a*, for HATC-05, was from the CDJ towards the outer edge of cementum, having the lowest value close to this latter. Therefore, it is feasible to presume that the changes in lattice parameter *a* for HATC-05 could also be related to ageing process, as it has been suggested (Foley et al., 2020).

The notion that the underlying characteristic of the incremental lines of AEFC is owing to an alternative pattern of hypo- and then hyper mineralization of the collagen fibres (Lieberman, 1994) or to the crystals' orientation and size (Cool et al., 2002) was not proven true from the results obtained in this research. Features like length, thickness and width of the apatite crystal features are highly correlated with crystal volume (Turunen et al., 2016), and that the variation of the size of the crystals is directly proportional to the crystallinity (Paschalis et al., 1996; Turunen et al., 2011). Therefore, the values obtained here for T- and L- parameters, helped us to interpret that across the entire length and width of the AEFC, the presence of arrayed and organized small crystals followed by larger ones, like the incremental lines, was not found and, thus neither were changes in the crystallinity that could point to a resemblance of an hypo- and hyper mineralization pattern.

3.5. XRF

The spatial distribution maps of Ca, P and Zn, of the five scanned samples are shown in Fig. 11. In accord with other investigations (Dean et al., 2018; Naji, Stock, et al., 2022; Stock et al., 2017) in all samples Ca and P distribution is widespread throughout cementum (AEFC and CIFC) and dentine, while Zn is registered only in cementum. However, contrary to what would be expected, the fluorescence of Ca and Zn did not show any evidence of incremental distribution that allows the visualization of the AEFC growth lines, as it has been reported (Dean et al., 2018); only two separated lines were identified for HATC-05. On the contrary, the Zn map for the CIFC sample (HATC-26) shows albeit weakly, some of the characteristic irregular incremental lines for cellular cementum. Regarding the intensity of variations of the elements (outlined profiles in Fig. 11), in all samples Zn shows the highest intensity peak at the outer edge of cementum followed by a drop and continuous variations of small scale, similar to what Naji and collaborators (2022) reported. The presence of Zn in cementum makes sense —bearing in mind the continuous growth by apposition of this mineralized tissue— and considering its important role in bone for the synthesis of the collagen matrix, mineralization, and bone turnover (Molenda & Kolmas, 2023). Furthermore, in growing bone high concentrations of the enzyme alkaline phosphatase (ALP), which Zn is part, has been found from that is fundamental for the mineralization process (Cho et al., 2007). In this sense, it has been documented that ALP along with pyrophosphate, are central for the formation of acellular cementum (Foster et al., 2012), which takes place at its outer edge, where the mineralization front is located (Bosshardt & Schroeder, 1991). Therefore, this reasoning, found also in other research (Dean et al., 2018; Naji, Stock, et al., 2022), explained why the highest Zn intensity is located at the outer edge of the cementum. On the other hand, the number of intensity peaks and drops for Ca and Zn, in the cases that present them, do not match the number of the incremental lines that it has been reported elsewhere for each of the samples (Couoh, 2017), and is contrary to what it has been suggested (Naji, Stock, et al., 2022).

The thickness of the samples used here (1 μm) might be the factor that caused the absence of any visualization of the AEFC incremental lines, in comparison with the ~ 100 μm used by Dean and collaborators (2018). Nevertheless, in this study the depth from which the elemental information is obtained, *i.e.*, 1 μm, provides certainty of the elements' signal intensity, which was not reduced because of the X-ray absorption in the material, as it occurred with thicker samples. Consequently, with this experiment, observing Ca and P distribution maps, it is clear that a linear pattern of hyper-hypo mineralization does not necessarily take place for tooth cementum. Furthermore, the complex arrangement of the collagen fibres, as shown with PFIB-SEM images, is slightly expressed on the resulting Ca and P spatial distribution maps of samples HATC-12, HATC-27 and HATC-05. Hence, on a thicker sample the XRF signals, from a greater depth, would likely show the composite structural information of the branched parallel fibres that constitute the AEFC incremental lines, as it has been detected with PFIB-SEM and differential interference contrast images. Conversely, because the structural organization of CIFC is consistent as a unit block (with a clear and constant alternating lamellar pattern (Yamamoto et al., 2026), even with 1 μm thickness it was possible to identify its incremental lines reflecting the alternating Zn intensities, which might point to a mineralization rhythm rather than different degrees of mineralization (Dean et al., 2018).

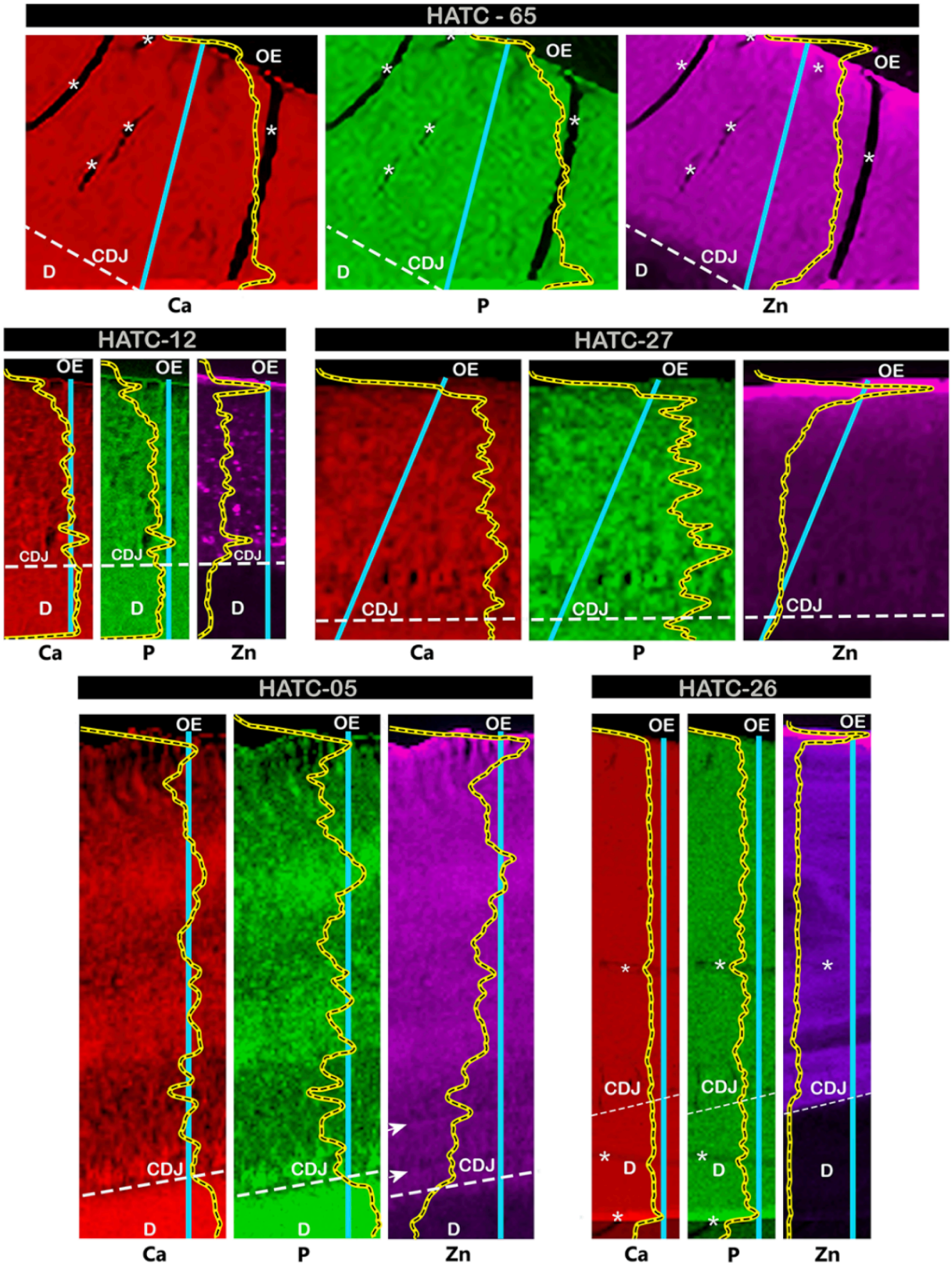

Fig. 11. XRF maps of Ca, P and Zn distribution. The overlapped longitudinal blue line (from the outer edge (OE), passing through the cemento-dentinal junction (CDJ) and reaching the dentine (D)) indicates the profile of intensities for each element. In HATC-05, white arrows in the Zn map point to (possible) incremental lines. The dashed white lines mark the division of cementum and dentine and the asterisk refers to folds in the sample. (For interpretation of the references to colour in this figure legend, the reader is referred to the web version of this article.)

4. Conclusions

Acellular extrinsic fibre cementum has probably been the least studied of the mineralized tissues and this research has opened up access to its complex structural organization. The use of multi-modal and multi-scale techniques allowed us to form a hierarchical perspective of the AEFC's organization. The structure that exists behind the appearance of the incremental alternating pattern —that is, visualized with polarized light microscopy— are branching Sharpey's fibres that constantly form aligned arched structures that are joined by these same fibres but in a parallel fashion. Additionally, the bright and dark alternating pattern, characteristic of the AEFC incremental lines, can be associated with the fibres' orientations, i.e., the parallel branched fibres and the perpendicular Sharpey's fibres sections that are among them. This mineral tissue is not organized by uniformed layers, otherwise, the Sharpey's fibres before branching out are laid out, not only on one orthogonal plane but crossing along two. Furthermore, the parallel fibres are not set as a continuum on the same plane and when they are superimposed project the incremental lines due to the collagen birefringence. This explain why AEFC cross-sections of different thicknesses can display mineralized collagen fibres with haphazard orientations. Consequently, the orientation of the apatite crystallites is dependent on the position of the collagen fibres. Significantly, no patterns of hyper/hypo mineralization were found, on the contrary, from the mineral point of view the tissue is relatively homogeneous. Therefore, no intrinsic characteristics of the mineral phase could be associated with the alternating AEFC incremental pattern. Significant challenges still remain in order to comprehend on the one hand, if there is a relevance of the arched structures formed by the Sharpey's branching fibres; and on the other hand, to understand in depth the presence of Zn within the mineral structure and the AEFC hierarchical organization.

CRediT authorship contribution statement

Lourdes R. Couoh: Writing – review & editing, Writing – original draft, Visualization, Validation, Methodology, Investigation, Funding acquisition, Formal analysis, Conceptualization. **Lauro Bucio:** Writing – review & editing, Methodology, Investigation, Formal analysis. **José Luis Ruvalcaba:** Writing – review & editing, Methodology, Investigation, Formal analysis. **Britta Manoel:** Writing – review & editing, Methodology, Investigation, Formal analysis. **Tengteng Tang:** Data curation, Methodology, Writing – review & editing. **Aurélien Gourrier:** Writing – review & editing, Methodology, Investigation, Formal analysis. **Kathryn Grandfield:** Writing – review & editing, Visualization, Validation, Supervision, Resources, Project administration, Methodology, Investigation, Funding acquisition, Formal analysis, Conceptualization.

Declaration of competing interest

The authors declare that they have no known competing financial interests or personal relationships that could have appeared to influence the work reported in this paper.

Data availability

No data was used for the research described in the article.

Acknowledgements

Postdoctoral Research Fellowship by CONACYT Mexico (application number 250642) was granted to LC. The Instituto Nacional de Antropología e Historia, México, supported LC with a granted research project (Sistema Institucional de Proyectos-31306 INAH-Mexico). Additional support provided by the Natural Sciences and Engineering Research Council of Canada Discovery Grant (RGPIN-2020-05722) to KG. Electron microscopy was performed at the Canadian Centre for Electron Microscopy at McMaster University, Canada. Beamtime was awarded on application number LS-25-21 to ID13 of the European Synchrotron Radiation Facility, France. Marcia Reid, Dakota Binkley and Xiaoyue Wang are acknowledge for technical assistance with sample preparation, electron tomography and synchrotron experiments, respectively. To J. Arturo Talavera from Dirección de Antropología Física INAH, México, for his valuable help in the acquisition of samples.

Appendix A. Supplementary material

Supplementary data to this article can be found online at https://doi.org/10.1016/j.jsb.2024.108084.

References

Aboulfadl, H., Hulliger, J., 2015. Absolute polarity determination of teeth cementum by phase sensitive second harmonic generation microscopy. J. Struct. Biol. 192 (1), 67–75. https://doi.org/10.1016/j.jsb.2015.08.011.

Akabane, C., Pabisch, S., Wagermaier, W., Roschger, A., Tobori, N., Okano, T., Murakami, S., Fratzl, P., Weinkamer, R., 2021. The effect of aging on the nanostructure of murine alveolar bone and dentin. J. Bone Miner. Metab. 39 (5), 757–768. https://doi.org/10.1007/s00774-021-01227-0.

Albéric, M., Dean, M.N., Gourrier, A., Wagermaier, W., Dunlop, J.W.C., Staude, A., Fratzl, P., Reiche, I., 2017. Relation between the macroscopic pattern of elephant ivory and its three-dimensional micro-tubular network. PLoS One 12 (1), 1–22. https://doi.org/10.1371/journal.pone.0166671.

Al-Jawad, M., Steuwer, A., Kilcoyne, S.H., Shore, R.C., Cywinski, R., Wood, D.J., 2007. 2D mapping of texture and lattice parameters of dental enamel. Biomaterials 28 (18), 2908–2914. https://doi.org/10.1016/j.biomaterials.2007.02.019.

Ashiotis, G., Deschildre, A., Nawaz, Z., Wright, J.P., Karkoulis, D., Picca, F.E., Kieffer, J., 2015. The fast azimuthal integration Python library: PyFAI. J. Appl. Cryst. 48, 510–519. https://doi.org/10.1107/S1600576715004306.

Benecke, G., Wagermaier, W., Li, C., Schwartzkopf, M., Flucke, G., Hoerth, R., Zizak, I., Burghammer, M., Metwalli, E., Müller-Buschbaum, P., Trebbin, M., Förster, S., Paris, O., Roth, S.V., Fratzl, P., 2014. A customizable software for fast reduction and analysis of large X-ray scattering data sets: Applications of the new DPDAK package to small-angle X-ray scattering and grazing-incidence small-angle X-ray scattering. J. Appl. Cryst. 47 (5), 1797–1803.

Berkovitz, B. K. B., Holland, G. R., & Moxham, B. J. (2018). *Oral Anatomy, Histology and Embriology* (Fifth). Elsevier. http://evolve.elsevier.com/Zachary/McGavin/.

Bertin, T.J.C., Thivichon-Prince, B., LeBlanc, A.R.H., Caldwell, M.W., Viriot, L., 2018. Current perspectives on tooth implantation, attachment, and replacement in amniota. Front. Physiol. 9 (NOV), 1–20. https://doi.org/10.3389/fphys.2018.01630.

Bertrand, B., Cunha, E., Bécart, A., Gosset, D., Hédouin, V., 2019. Age at death estimation by cementochronology: Too precise to be true or too precise to be accurate? Am. J. Phys. Anthropol. 169 (3), 464–481. https://doi.org/10.1002/ajpa.23849.

Bilgin, E., Gürgan, C.A., Arpak, M.N., Bostanci, H.S., Güven, K., 2004. Morphological changes in diseased cementum layers: A scanning electron microscopy study. Calcif. Tissue Int. 74 (5), 476–485. https://doi.org/10.1007/s00223-003-0195-1.

Binkley, D.M., Deering, J., Yuan, H., Gourrier, A., Grandfield, K., 2020. Ellipsoidal mesoscale mineralization pattern in human cortical bone revealed in 3D by plasma focused ion beam serial sectioning. J. Struct. Biol. 212 (2), 107615 https://doi.org/10.1016/j.jsb.2020.107615.

Bosshardt, D., 2005. Are cementoblasts a subpopulation of osteoblasts or a unique phenotype? J. Dent. Res. 84 (5), 390–406. https://doi.org/10.1177/154405910508400501.

Bosshardt, D., & Sculean, A. (2009). Does periodontal tissue regeneration really work? *Periodontol 2000*, *51*(ii), 208–219.

Bosshardt, D.D., Schroeder, H.E., 1991. Establishment of acellular extrinsic fiber cementum on human teeth. Cell Tissue Res. 263 (263), 325–336.

Bosshardt, D., Schroeder, H., 1992. Initial formation of cellular intrinsic fiber cementum in developing human teeth. A light- and electron-microscopic study. Cell Tissue Res. 267 (2), 321–335.

Bosshardt, D.D., Schroeder, H.E., 1996. Cementogenesis reviewed: A comparison between human premolars and rodent molars. Anat. Rec. 245 (2), 267–292. https://doi.org/10.1002/(SICI)1097-0185(199606)245:2<267::AID-AR12>3.0.CO;2-N.

Bosshardt, D., Selvig, K., 1997. Dental cementum: the dynamic tissue covering of the root. Periodontology 2000 (13), 41–75.

Casanova, E.A., Rodriguez-Palomo, A., Stähli, L., Arnke, K., Gröninger, O., Generali, M., Neldner, Y., Tiziani, S., Dominguez, A.P., Guizar-Sicairos, M., Gao, Z., Appel, C., Nielsen, L.C., Georgiadis, M., Weber, F.E., Stark, W., Pape, H.C., Cinelli, P., Liebi, M., 2023. SAXS imaging reveals optimized osseointegration properties of bioengineered oriented 3D-PLGA/aCaP scaffolds in a critical size bone defect model. Biomaterials 294 (January). https://doi.org/10.1016/j.biomaterials.2022.121989.

Catros, S., Pothuaud, L., Dard, M., Fricain, J.-C., 2008. Collagen fibrils of human Acellular extrinsic fiber cementum. J. Periodontol. 79 (6), 1095–1100. https://doi.org/10.1902/jop.2008.070482.

Cho, Y.-E., Lomeda, R.-A.-R., Ryu, S.-H., Sohn, H.-Y., Shin, H.-I., Beattie, J.H., Kwun, I.-S., 2007. Zinc deficiency negatively affects alkaline phosphatase and the

concentration of Ca, Mg and P in rats. Nutr. Res. Pract. 1 (2), 113. https://doi.org/10.4162/nrp.2007.1.2.113.
Colard, T., Falgayrac, G., Bertrand, B., Naji, S., Devos, O., Balsack, C., Delannoy, Y., Penel, G., 2016. New insights on the composition and the structure of the acellular extrinsic fiber cementum by Raman analysis. PLoS One 11 (12), 1–20.
Cool, S.M., Forwood, M.R., Campbell, P., Bennett, M.B., 2002. Comparisons between bone and cementum compositions and the possible basis for their layered appearances. Bone 30 (2), 386–392. https://doi.org/10.1016/S8756-3282(01)00686-X.
Couoh, L.R., 2017. Differences between biological and chronological age-at-death in human skeletal remains: A change of perspective. Am. J. Phys. Anthropol. 163 (4), 671–695. https://doi.org/10.1002/ajpa.23236.
de Jong, T., Bakker, A.D., Everts, V., Smit, T.H., 2017. The intricate anatomy of the periodontal ligament and its development: Lessons for periodontal regeneration. J. Periodontal Res. 52 (6), 965–974. https://doi.org/10.1111/jre.12477.
Dean, C., LeCabec, A., Spiers, K., Zhang, Y., Garrevoet, J., 2018. Incremental distribution of strontium and zinc in great ape and fossil hominin cementum using synchrotron X-ray fluorescence mapping. J. R. Soc. Interface 15 (138). https://doi.org/10.1098/rsif.2017.0626.
Duailibi, S. E., Duailibi, M. T., Vacanti, J. P., & Yelick, P. C. (2006). Prospects for tooth regeneration. *Periodontology 2000*, *41*(1), 177–187.
Elliot J. C. (1994). Structure and Chemistry of the Apatites and Other Calcium Orthophosphates. Else.
Foley, B., Greiner, M., McGlynn, G., Schmahl, W.W., 2020. Anatomical variation of human bone bioapatite crystallography. Crystals 10 (10), 1–25. https://doi.org/10.3390/cryst10100859.
Foster, B.L., Nagatomo, K.J., Nociti, F.H., Fong, H., Dunn, D., Tran, A.B., Wang, W., Narisawa, S., Millán, J.L., Somerman, M.J., 2012. Central role of pyrophosphate in acellular cementum formation. PLoS One 7 (6).
Fratzl, P., Fratzl-Zelman, N., Klaushofer, K., Vogl, G., Koller, K., 1991. Nucleation and growth of mineral crystals in bone studied by small-angle X-ray scattering. Calcif. Tissue Int. 48 (6), 407–413. https://doi.org/10.1007/BF02556454.
Fratzl, P., Groschner, M., Vogl, G., Plenk, H., Eschberger, J., Fratzl-Zelman, N., Koller, K., Klaushofer, K., 1992. Mineral crystals in calcified tissues: A comparative study by SAXS. J. Bone Miner. Res. 7 (3), 329–334. https://doi.org/10.1002/jbmr.5650070313.
Fratzl, P., Schreiber, S., Klaushofer, K., 1996. Bone mineralization as studied by small-angle X-ray scattering. Connect. Tissue Res. 34, 247–254.
Fratzl, P., Gupta, H.S., Paschalis, E.P., Roschger, P., 2004. Structure and mechanical quality of the collagen-mineral nano-composite in bone. J. Mater. Chem. 14 (14), 2115–2123. https://doi.org/10.1039/b402005g.
Fratzl-Zelman, N., Schmidt, I., Roschger, P., Glorieux, F.H., Klaushofer, K., Fratzl, P., Rauch, F., Wagermaier, W., 2014. Mineral particle size in children with osteogenesis imperfecta type I is not increased independently of specific collagen mutations. Bone 60 (2), 122–1128. https://doi.org/10.1016/j.bone.2013.11.023.
Furseth, R., 1974. The fine structure of acellular cementum in young human premolars. Scand. J. Dent. Res. 82 (6), 437–441. https://doi.org/10.1111/j.1600-0722.1974.tb00398.x.
Giraud-Guille, M.M., 1988. Twisted plywood architecture of collagen fibrils in human compact bone osteons. Calcif. Tissue Int. 42 (3), 167–180. https://doi.org/10.1007/BF02556330.
Gourrier, A., Li, C., Siegel, S., Paris, O., Roschger, P., Klaushofer, K., Fratzl, P., 2010. Scanning small-angle X-ray scattering analysis of the size and organization of the mineral nanoparticles in fluorotic bone using a stack of cards model. J. Appl. Cryst. 43 (6), 1385–1392. https://doi.org/10.1107/S0021889810035090.
Gourrier, A., Chadefaux, C., Lemaitre, E., Bellot-Gurlet, L., Reynolds, M., Burghammer, M., Plazanet, M., Boivin, G., Farlay, D., Bunk, O., Reiche, I., 2017. Nanoscale modifications in the early heating stages of bone are heterogeneous at the microstructural scale. PLoS One 12 (4), 1–23. https://doi.org/10.1371/journal.pone.0176179.
Grandfield, K., Engqvist, H., 2014. Characterization of dental interfaces with electron tomography. Biointerphases 9 (2), 029001. https://doi.org/10.1116/1.4862096.
Grandfield, K., Vuong, V., Schwarcz, H.P., 2018. Ultrastructure of bone: Hierarchical features from nanometer to micrometer scale revealed in focused ion beam sections in the TEM. Calcif. Tissue Int. 103 (6), 606–616. https://doi.org/10.1007/s00223-018-0454-9.
Grant, D., Bernick, S., 1972. Formation of the periodontal ligament. J. Periodontol. 43 (1), 17–25. https://doi.org/10.1902/jop.1972.43.1.17.
Hand, A.R., Frank, M.E., 2014. Fundamentals of Oral Histology and Physiology. John Wiley & Sons Inc.
Hinrichs, C., Nicklisch, N., Mardare, C.C., Orechovski, B., Hassel, A.W., Kleber, C., Alt, K. W., 2022. Incremental lines in human acellular tooth cementum – New insights by SEM analysis. Ann. Anat. 243, 151933 https://doi.org/10.1016/j.aanat.2022.151933.
Hirashima, S., Ohta, K., Kanazawa, T., Okayama, S., Togo, A., Miyazono, Y., Kusukawa, J., & Nakamura, K. ichiro. (2020). Three-dimensional ultrastructural analysis and histomorphometry of collagen bundles in the periodontal ligament using focused ion beam/scanning electron microscope tomography. *Journal of Periodontal Research*, *55* (1), 23–31. DOI: 10.1111/jre.12592.
Hirashima, S., Ohta, K., Kanazawa, T., Togo, A., Kakuma, T., Kusukawa, J., Nakamura, K., 2019. Three-dimensional ultrastructural and histomorphological analysis of the periodontal ligament with occlusal hypofunction via focused ion beam/scanning electron microscope tomography. Sci. Rep. 9 (1), 1–11. https://doi.org/10.1038/s41598-019-45963-w.
Hirashima, S., Kanazawa, T., Ohta, K., Nakamura, K., 2020b. Three-dimensional ultrastructural imaging and quantitative analysis of the periodontal ligament. Anat. Sci. Int. 95, 1–11. https://doi.org/10.1007/s12565-019-00502-5.
Hirashima, S., Ohta, K., Kanazawa, T., Togo, A., Tsuneyoshi, R., Kusukawa, J., Nakamura, K.I., 2020c. Cellular network across cementum and periodontal ligament elucidated by FIB/SEM tomography. Microscopy 69 (1), 53–58. https://doi.org/10.1093/jmicro/dfz117.
Ho, S.P., Yu, B., Yun, W., Marshall, G.W., Ryder, M.I., Marshall, S.J., 2009. Structure, chemical composition and mechanical properties of human and rat cementum and its interface with root dentin. Acta Biomater. 5 (2), 707–718. https://doi.org/10.1016/j.actbio.2008.08.013.
Ho, S.P., Kurylo, M.P., Fong, T.K., Lee, S.S.J.J., Wagner, H.D., Ryder, M.I., Marshall, G. W., 2010. The biomechanical characteristics of the bone-periodontal ligament-cementum complex. Biomaterials 31 (25), 6635–6646. https://doi.org/10.1016/j.biomaterials.2010.05.024.
Jantou, V., Turmaine, M., West, G.D., Horton, M.A., McComb, D.W., 2009. Focused ion beam milling and ultramicrotomy of mineralised ivory dentine for analytical transmission electron microscopy. Micron 40 (4), 495–501. https://doi.org/10.1016/j.micron.2008.12.002.
Kallaste, T., Nemliher, J., 2005. Apatite varieties in extant and fossil vertebrate mineralized tissues. J. Appl. Cryst. 38 (4), 587–594. https://doi.org/10.1107/S0021889805011404.
Kannan, S., Goetz-Neunhoeffer, F., Neubauer, J., Ferreira, J.M.F., 2008. Ionic substitutions in biphasic hydroxyapatite and β-tricalcium phosphate mixtures: Structural analysis by rietveld refinement. J. Am. Ceram. Soc. 91 (1), 1–12. https://doi.org/10.1111/j.1551-2916.2007.02117.x.
Kay, M.I., Young, R.A., Posner, A.S., 1964. Crystal structure of hysroxyapatite. Nature 204, 1050–1052.
Kieffer, J., Karkoulis, D., 2013. PyFAI, a versatile library for azimuthal regrouping. J. Phys. Conf. Ser. 425 (PART 20) https://doi.org/10.1088/1742-6596/425/20/202012.
Kieffer, J., Wright, J.P., 2013. PyFAI: A python library for high performance azimuthal integration on GPU. Powder Diffr. 28 (SUPPL.2), 3–10. https://doi.org/10.1017/S0885715613000924.
Kvam, E., 1973. Topography of principal fibers. Scand. J. Dent. Res. 81, 553–557. https://doi.org/10.1111/j.1600-0722.1973.tb00365.x.
Lange, C., Li, C., Manjubala, I., Wagermaier, W., Kühnisch, J., Kolanczyk, M., Mundlos, S., Knaus, P., Fratzl, P., 2011. Fetal and postnatal mouse bone tissue contains more calcium than is present in hydroxyapatite. J. Struct. Biol. 176 (2), 159–167. https://doi.org/10.1016/j.jsb.2011.08.003.
LeBlanc, A.R.H., Reisz, R.R., 2013. Periodontal ligament, cementum, and Alveolar bone in the oldest herbivorous tetrapods, and their evolutionary significance. PLoS One 8 (9). https://doi.org/10.1371/journal.pone.0074697.
Lieberman, D.E., 1994. The biological basis for seasonal increments in dental cementum and their application to archaeologicl research. J. Archaeol. Sci. 21, 525–539.
Loeber, T.H., Laegel, B., Wolff, S., Schuff, S., Balle, F., Beck, T., Eifler, D., Fitschen, J.H., Steidl, G., 2017. Reducing curtaining effects in FIB/SEM applications by a goniometer stage and an image processing method. J. Vac. Sci. Technol., B: Nanotechnol. Microelectron.: Mater., Process., Meas., Phenom. 35 (6), 06GK01. https://doi.org/10.1116/1.4991638.
Märten, A., Fratzl, P., Paris, O., Zaslansky, P., 2010. On the mineral in collagen of human crown dentine. Biomaterials 31 (20), 5479–5490. https://doi.org/10.1016/j.biomaterials.2010.03.030.
McCulloch, C.A.G., Lekic, P., McKee, M.D., 2000. Role of physical forces in regulating the form and function of. Periodontology 2000 (24), 56–72.
McNally, E.A., Schwarcz, H.P., Botton, G.A., Arsenault, A.L., 2012. A model for the ultrastructure of bone based on electron microscopy of ion-milled sections. PLoS One 7 (1), 1–12. https://doi.org/10.1371/journal.pone.0029258.
Molenda, M., Kolmas, J., March. 2023. The role of zinc in bone tissue health and regeneration—A review. Biol. Trace Elem. Res. https://doi.org/10.1007/s12011-023-03631-1.
Morgan, H., Wilson, R.M., Elliott, J.C., Dowker, S.E.P., Anderson, P., 2000. Preparation and characterisation of monoclinic hydroxyapatite and its precipitated carbonate apatite intermediate. Biomaterials 21 (6), 617–627. https://doi.org/10.1016/S0142-9612(99)00225-2.
Naji, S., Colard, T., Blondiaux, J., Bertrand, B., d'Incau, E., Bocquet-Appel, J.P., 2016. Cementochronology, to cut or not to cut? Int. J. Paleopathol. 15, 113–119. https://doi.org/10.1016/j.ijpp.2014.05.003.
Naji, S., Rendu, W., & Gourichon, L. (2022). *Dental Cementum in Anthropology* (S. Naji, W. Rendu, & L. Gourichon, Eds.). Cambridge University Press. DOI: 10.1017/9781108569507.
Naji, S., Stock, S.R., Rendu, W., Gourichon, L., Colard, T., Cai, Z., 2022. Recent advances on acellular cementum increments composition using synchrotron X-radiation. In: Naji, S., Rendu, W., Gourichon, L. (Eds.), Dental Cementum in Anthropology. Cambridge University, pp. 110–137. https://doi.org/10.1017/9781108569507.008.
Pabisch, S., Wagermaier, W., Zander, T., Li, C., Fratzl, P., 2013. Imaging the nanostructure of bone and dentin through small- and wide-angle X-ray scattering. In: Methods in Enzymology, 532. Academic Press Inc., pp. 391–413. https://doi.org/10.1016/B978-0-12-416617-2.00018-7
Paschalis, E.P., DiCarlo, E., Betts, F., Sherman, P., Mendelsohn, R., Boskey, A.L., 1996. FTIR microspectroscopic analysis of human osteonal bone. Calcif. Tissue Int. 59 (6), 480–487. https://doi.org/10.1007/BF00369214.
Raspanti, M., Cesari, C., De Pasquale, V., Ottani, V., Strocchi, R., Zucchelli, G., Ruggeri, A., 2000. A histological and electron-microscopic study of the architecture and ultrastructure of human periodontal tissues. Arch. Oral Biol. 45 (3), 185–192. https://doi.org/10.1016/S0003-9969(99)00145-4.

Ratnayake, J.T.B., Mucalo, M., Dias, G.J., 2017. Substituted hydroxyapatites for bone regeneration: A review of current trends. J. Biomed. Mater. Res. - Part B Appl. Biomater. 105 (5), 1285–1299. https://doi.org/10.1002/jbm.b.33651.

Reznikov, N., Almany-Magal, R., Shahar, R., Weiner, S., 2013. Three-dimensional imaging of collagen fibril organization in rat circumferential lamellar bone using a dual beam electron microscope reveals ordered and disordered sub-lamellar structures. Bone 52 (2), 676–683. https://doi.org/10.1016/j.bone.2012.10.034.

Reznikov, N., Shahar, R., Weiner, S., 2014. Three-dimensional structure of human lamellar bone: The presence of two different materials and new insights into the hierarchical organization. Bone 59, 93–104. https://doi.org/10.1016/j.bone.2013.10.023.

Roschger, P., Grabner, B.M., Rinnerthaler, S., Tesch, W., Kneissel, M., Berzlanovich, A., Klaushofer, K., Fratzl, P., 2001. Structural development of the mineralized tissue in the human L4 vertebral body. J. Struct. Biol. 136 (2), 126–136. https://doi.org/10.1006/jsbi.2001.4427.

Ryan, J., Stulajter, M.M., Okasinski, J.S., Cai, Z., Gonzalez, G.B., Stock, S.R., 2020. Carbonated apatite lattice parameter variation across incremental growth lines in teeth. Materialia 14 (May), 100935. https://doi.org/10.1016/j.mtla.2020.100935.

Schwarcz, H.P., Binkley, D.M., Luo, L., Grandfield, K., 2020. A search for apatite crystals in the gap zone of collagen fibrils in bone using dark-field illumination. Bone 135 (6), 115304. https://doi.org/10.1016/j.bone.2020.115304.

Selvig, K.A., 1965. The fine structure of human cementum. Acta Odontol. Scand. 23 (4), 423–441. https://doi.org/10.3109/00016356509007523.

Solé, V.A., Papillon, E., Cotte, M., Walter, P., Susini, J., 2007. A multiplatform code for the analysis of energy-dispersive X-ray fluorescence spectra. Spectrochim. Acta - Part B Atomic Spectrosc. 62 (1), 63–68. https://doi.org/10.1016/j.sab.2006.12.002.

Stock, S.R., Finney, L.A., Telser, A., Maxey, E., Vogt, S., Okasinski, J.S., 2017. Cementum structure in Beluga whale teeth. Acta Biomater. 48, 289–299. https://doi.org/10.1016/j.actbio.2016.11.015.

Stutz, A.J., 2002. Polarizing microscopy identification of chemical diagenesis in archaeological cementum. J. Archaeol. Sci. 29 (11), 1327–1347. https://doi.org/10.1006/jasc.2001.0805.

Toby, B.H., von Dreele, R.B., 2013. GSAS-II: The genesis of a modern open-source all purpose crystallography software package. J. Appl. Cryst. 46 (2), 544–549. https://doi.org/10.1107/S0021889813003531.

Turunen, M.J., Saarakkala, S., Rieppo, L., Helminen, H.J., Jurvelin, J.S., Isaksson, H., 2011. Comparison between infrared and raman spectroscopic analysis of maturing rabbit cortical bone. Appl. Spectrosc. 65 (6), 595–603. https://doi.org/10.1366/10-06193.

Turunen, M.J., Kaspersen, J.D., Olsson, U., Guizar-Sicairos, M., Bech, M., Schaff, F., Tägil, M., Jurvelin, J.S., Isaksson, H., 2016. Bone mineral crystal size and organization vary across mature rat bone cortex. J. Struct. Biol. 195 (3), 337–344. https://doi.org/10.1016/j.jsb.2016.07.005.

Wagermaier, W., Gourrier, A.A., Aichmayer, B., 2013. Understanding hierarchy and functions of bone using scanning x-ray scattering methods. In: Fratzl, P., Dunlop, J. W.C., Weinkamer, R. (Eds.), Materials Design Inspired by Nature : Function through Inner Architecture, 1st ed. Royal Society of Chemistry, pp. 1–30.

Wilson, R.M., Elliott, J.C., Dowker, S.E.P., 1999. Rietveld refinement of the crystallographic structure of human dental enamel apatites. Am. Mineral. 84 (9), 1406–1414. https://doi.org/10.2138/am-1999-0919.

Xi, L., Zhang, Y., Gupta, H., Terrill, N., Wang, P., Zhao, T., Fang, D., 2021. A multiscale study of structural and compositional changes in a natural nanocomposite: Osteoporotic bone with chronic endogenous steroid excess. Bone 143. https://doi.org/10.1016/j.bone.2020.115666.

Yamamoto, T., Domon, T., Takahashi, S., Suzuki, R., Islam, M.N., 2000. The fibrillar structure of cement lines on resorbed root surfaces of human teeth. J. Periodont. Res. 35 (4), 208–213.

Yamamoto, T., Li, M., Liu, Z., Guo, Y., Hasegawa, T., Masuki, H., Suzuki, R., Amizuka, N., 2010. Histological review of the human cellular cementum with special reference to an alternating lamellar pattern. Odontology 98 (2), 102–109.

Yamamoto, T., Hasegawa, T., Yamamoto, T., Hongo, H., Amizuka, N., 2016. Histology of human cementum: Its structure, function, and development. Japanese Dent. Sci. Rev. 52 (3), 63–74. https://doi.org/10.1016/j.jdsr.2016.04.002.